

1 Suppressive myeloid cells are a hallmark of 2 severe COVID-19

3 Jonas Schulte-Schrepping^{1*}, Nico Reusch^{1*}, Daniela Paclik^{2*}, Kevin Baßler^{1*}, Stephan
4 Schlickeiser^{3*}, Bowen Zhang^{4*}, Benjamin Krämer^{5*}, Tobias Krammer^{6*}, Sophia Brumhard^{7*},
5 Lorenzo Bonaguro^{1*}, Elena De Domenico^{8*}, Daniel Wendisch^{7*}, Martin Grasshoff⁴, Theodore S.
6 Kapellos¹, Michael Beckstette⁴, Tal Pecht¹, Adem Saglam⁸, Oliver Dietrich⁶, Henrik E. Mei⁹, Axel
7 R. Schulz⁹, Claudia Conrad⁷, Désirée Kunkel¹⁰, Ehsan Vafadarnejad⁶, Cheng-Jian Xu^{4,11}, Arik
8 Horne¹, Miriam Herbert¹, Anna Drews⁸, Charlotte Thibeault⁷, Moritz Pfeiffer⁷, Stefan
9 Hippenstiel^{7,12}, Andreas Hocke^{7,12}, Holger Müller-Redetzky⁷, Katrin-Moira Heim⁷, Felix Machleidt⁷,
10 Alexander Uhrig⁷, Laure Bousquillon de Jarcy⁷, Linda Jürgens⁷, Miriam Stegemann⁷, Christoph
11 R. Glösenkamp⁷, Hans-Dieter Volk^{2,3,13}, Christine Goffinet^{14,15}, Jan Raabe⁵, Kim Melanie Kaiser⁵,
12 Michael To Vinh⁵, Gereon Rieke⁵, Christian Meisel¹⁴, Thomas Ulas⁸, Matthias Becker⁸, Robert
13 Geffers¹⁶, Martin Witzzenrath^{7,12}, Christian Drosten^{14,19}, Norbert Suttorp^{7,12}, Christof von Kalle¹⁷,
14 Florian Kurth^{7,18}, Kristian Händler⁸, Joachim L. Schultze^{1,8,#,\$}, Anna C Aschenbrenner^{20,#}, Yang
15 Li^{4,#}, Jacob Nattermann^{5,19,#}, Birgit Sawitzki^{2,#}, Antoine-Emmanuel Saliba^{6,#}, Leif Erik Sander^{7,12#},
16 Deutsche COVID-19 OMICS Initiative (DeCOI)

17 * shared first authors, # shared last authors, \$ corresponding author

18 Affiliations

19
20 1 Life & Medical Sciences (LIMES) Institute, University of Bonn, Germany
21 2 Institute of Medical Immunology, Charité, Universitätsmedizin Berlin, Berlin, Germany
22 3 Institute of Medical Immunology, Charité, Universitätsmedizin Berlin, Berlin, Germany & BIH Center
23 for Regenerative Therapies, Charité and Berlin Institute of Health, Charité, Universitätsmedizin
24 Berlin, Berlin, Germany.
25 4 Centre for Individualised Infection Medicine (CiiM) & TWINCORE, joint ventures between the
26 Helmholtz-Centre for Infection Research (HZI) and the Hannover Medical School (MHH), Hannover,
27 Germany
28 5 Department of Internal Medicine I, University Hospital Bonn, Bonn Germany
29 6 Helmholtz Institute for RNA-based Infection Research (HIRI), Helmholtz-Center for Infection
30 Research (HZI), Würzburg, Germany
31 7 Department of Infectious Diseases and Respiratory Medicine, Charité Universitätsmedizin Berlin,
32 Berlin, Germany
33 8 PRECISE Platform for Single Cell Genomics and Epigenomics, German Center for
34 Neurodegenerative Diseases, Bonn, Germany and University of Bonn, Bonn Germany
35 9 Mass Cytometry Lab, DRFZ Berlin, a Leibniz Institute, Berlin, Germany
36 10 Flow & Mass Cytometry Core Facility, Charité Universitätsmedizin Berlin and Berlin Institute of Health
37 (BIH), Berlin, Germany
38 11 Department of Internal Medicine and Radboud Center for Infectious Diseases, Radboud University
39 Medical Center, Nijmegen, the Netherlands
40 12 German Center for Lung Research (DZL)

41 13 Institute of Medical Immunology, Charité, Universitätsmedizin Berlin, Berlin, Germany, Labor Berlin-
42 Charité Vivantes, Department of Immunology, Berlin, Germany
43 14 Institute of Virology, Charité Universitätsmedizin Berlin, Berlin, Germany
44 15 Berlin Institute of Health, 10178 Berlin, Germany
45 16 Genome Analytics, Helmholtz-Center for Infection Research (HZI), Braunschweig, Germany
46 17 Clinical Study Center (CSC), Berlin Institute of Health (BIH), and Charite Universitätsmedizin Berlin,
47 Germany
48 18 Department of Tropical Medicine, Bernhard Nocht Institute for Tropical Medicine & I. Department of
49 Medicine, University Medical Center Hamburg-Eppendorf, Hamburg, Germany
50 19 German Center for Infection Research (DZIF)
51 20 Life & Medical Sciences (LIMES) Institute, University of Bonn, Germany and Radboud UMC,
52 Nijmegen, The Netherlands

53

54

55

56

57

58 **Key Words:**

59 COVID-19, SARS-CoV-2, monocytes, immunosuppressive neutrophils, neutrophils,
60 immunosuppressive neutrophils, scRNA-seq, mass cytometry, CyTOF

61

62 Abstract

63 'Severe Acute Respiratory Syndrome - Coronavirus-2' (SARS-CoV-2) infection causes
64 Coronavirus Disease 2019 (COVID-19), a mild to moderate respiratory tract infection in the
65 majority of patients. A subset of patients, however, progresses to severe disease and respiratory
66 failure with acute respiratory distress syndrome (ARDS). Severe COVID-19 has been associated
67 with increased neutrophil counts and dysregulated immune responses. The mechanisms of
68 protective immunity in mild forms and the pathogenesis of dysregulated inflammation in severe
69 courses of COVID-19 remain largely unclear. Here, we combined two single-cell RNA-sequencing
70 technologies and single-cell proteomics in whole blood and peripheral blood mononuclear cells
71 (PBMC) to determine changes in immune cell composition and activation in two independent dual-
72 center patient cohorts (n=46+n=54 COVID-19 samples), each with mild and severe cases of
73 COVID-19. We observed a specific increase of HLA-DR^{hi}CD11c^{hi} inflammatory monocytes that
74 displayed a strong interferon (IFN)-stimulated gene signature in patients with mild COVID-19,
75 which was absent in severe disease. Instead, we found evidence of emergency myelopoiesis,
76 marked by the occurrence of immunosuppressive pre-neutrophils and immature neutrophils and
77 populations of dysfunctional and suppressive mature neutrophils, as well as suppressive HLA-
78 DR^{lo} monocytes in severe COVID-19. Our study provides detailed insights into systemic immune
79 response to SARS-CoV-2 infection and it reveals profound alterations in the peripheral myeloid
80 cell compartment associated with severe courses of COVID-19.

81
82
83

84 Introduction

85 The emergence of severe acute respiratory syndrome coronavirus 2 (SARS-CoV-2) in December
86 of 2019 (Wu et al., 2020) and the subsequent pandemic spread of Coronavirus Disease 2019
87 (COVID-19) has caused immense morbidity and mortality around the world (Fauver et al., 2020;
88 Zhou et al., 2020b). Clinical presentations of COVID-19 are variable, and while the majority of
89 patients experiences mild to moderate symptoms, a subset of 10-20% of patients develops
90 pneumonia and severe disease (Brignola et al., 1988; Guan et al., 2020a; Huang et al., 2020;
91 Wang et al., 2020b; Zhou et al., 2020a). Clinical deterioration and development of respiratory
92 failure and acute respiratory distress syndrome (ARDS), typically develops in the second week of
93 disease. Besides protracted viral replication, this kinetic suggests a role for secondary immune
94 responses in the development of severe COVID-19 (Ziying Ong et al., 2020). However, the exact
95 mechanisms that govern the pathophysiology of the different disease courses of COVID-19
96 remain ill-defined. Patients with comorbidities, including hypertension, diabetes, COPD,
97 cardiovascular disease, and cerebrovascular disease are at highest risk to develop severe
98 COVID-19 (Guan et al., 2020b; Wang et al., 2020a). Given that these conditions are associated
99 with chronic inflammation, disease severity of COVID-19 might be closely linked to the underlying
100 specific and nonspecific immune response to the virus.

101
102 SARS-CoV-2 was identified as the causative agent of COVID-19 (Wu et al., 2020) and similar to
103 SARS coronavirus, it uses ACE2 as the primary cellular entry receptor (Hoffmann et al., 2020; Li
104 et al., 2003). SARS-CoV-2 has a tropism for the upper airways and the lung (Wölfel et al., 2020),
105 despite rather low numbers of cells that co-express ACE2 and the essential cofactor for ACE2
106 binding, TMPRSS2 (Allan et al., 2020; Qi et al., 2020; Sungnak et al., 2020; Ziegler et al., 2020),
107 but the expression of ACE2 and TMPRSS2 in airway epithelial cells are increased by type-I IFN
108 stimulation (Ziegler et al., 2020). Single cell studies of bronchoalveolar lavage samples have
109 suggested a complex dysregulation of the pulmonary immune response in severe COVID-19 (Liao
110 et al., 2020). Overall, systemic inflammation is linked to an unfavorable clinical course of disease
111 and the development of severe COVID-19 (Giamarellos-Bourboulis et al., 2020; Ziying Ong et al.,
112 2020). SARS-CoV2 infection induces specific T cell and B cell responses, which is reflected by
113 elevation of SARS-CoV-2 peptide-specific T cells (Braun et al., 2020; Grifoni et al., 2020) and the
114 production of SARS-CoV-2 specific antibody responses (Long et al., 2020; Ni et al., 2020).
115 Patients with severe COVID-19 have high systemic levels of inflammatory cytokines, specifically
116 IL-1 β and IL-6 (Chen et al., 2020; Giamarellos-Bourboulis et al., 2020; Ziying Ong et al., 2020),
117 whereas interferon (IFN) responses appear to be impaired as shown by whole blood
118 transcriptomics (Hadjadj et al., 2020). Clinical observations and several studies indicate an
119 increase of neutrophils and a decrease of non-classical (CD14^{lo}CD16^{hi}) monocytes in severe
120 COVID-19 (Hadjadj et al., 2020; Merad and Martin, 2020). Severe immune dysregulation is a
121 common phenomenon in sepsis, characterized by a progression from hyperinflammatory states
122 to immunosuppression (Remy et al., 2020; Ritchie and Singanayagam, 2020) and similar
123 mechanisms have been proposed for severe COVID-19 (Giamarellos-Bourboulis et al., 2020), yet
124 mechanistic insights are still missing. Exacerbated immune responses play a major role in the
125 pathophysiology of SARS, leading to severe lung injury and respiratory failure (Perlman and
126 Dandekar, 2005). Mitigation of immunodysregulation could thus represent a major therapeutic

127 avenue for the treatment and prevention of severe COVID-19 (Dimopoulos et al., 2020; Jamilloux
128 et al., 2020). An early report investigating transcriptional profiles of peripheral blood mononuclear
129 cells (PBMC) of 7 patients with mixed clinical courses of COVID-19, revealed complex immune
130 deviations with changes in numerous cellular compartments, including monocytes, NK cells,
131 dendritic cells and T cells (Salomé and Mahmood, 2020; Wilk et al., 2020).

132
133 The heterogeneity of clinical phenotypes and the complexity of systemic immune responses to
134 COVID-19 highlight the need for detailed insights into different stages of the disease using high-
135 resolution techniques and well-characterized clinical cohorts. Here, we hypothesized that distinct
136 immune responses, particularly within the innate immune cell compartment, underlie the different
137 clinical trajectories of COVID-19 patients (McKechnie and Blish, 2020). The striking alterations in
138 cell counts and activation states of different innate immune cells in COVID-19 patients, and their
139 relation to disease severity are currently not sufficiently understood. Here, we performed single-
140 cell transcriptomics and single-cell proteomics on blood samples from two independent cohorts
141 of COVID-19 patients, which allowed for instant cross-validation of immunological findings.
142 COVID-19 patients with mild disease courses in both cohorts showed increased CD14⁺HLA-
143 DR^{hi}CD11c^{hi} inflammatory monocytes, which were marked by a strong IFN-stimulated gene
144 (ISG⁺) signature. In contrast, severe COVID-19 was associated with the appearance of immature
145 CD14⁺MPO⁺Ki67⁺HLA-DR^{lo} ISG⁺ suppressive monocytes and dysfunctional low-density
146 neutrophils. The latter were identified as ARG1⁺MPO⁺BPI⁺ pre-neutrophils and
147 ARG1⁺CD101⁺S100A8/A9⁺ immature neutrophils, indicative of emergency myelopoiesis. In
148 addition, suppressive PD-L1⁺CD123⁺ neutrophils were detected at late stages in severe COVID-
149 19. Collectively, our study links highly dysregulated myeloid cell responses to severe disease
150 courses of COVID-19.

151 Results

152 153 Dual center cohort study to assess immunological alterations in COVID-19 patients

154 In order to gain detailed insights into the distinct immunological events in mild *versus* severe
155 COVID-19, we analyzed peripheral blood samples collected from independent cohorts of COVID-
156 19 patients at two university medical centers in Germany. Samples from the Berlin cohort (cohort
157 1) were analyzed by mass cytometry (CyTOF) and single-cell RNA-sequencing (scRNA-seq)
158 using a droplet-based single cell platform (10x Chromium), while samples from the Bonn cohort
159 (cohort 2) were analyzed by multi-colour flow cytometry (MCFC) and scRNA-seq using a
160 microwell-based system (BD Rhapsody). We profiled a total of 8.1 million cells by their surface
161 protein markers and over 210,000 cells by scRNA-seq in 131 samples derived from a total of 33

162 COVID-19 patients and 23 controls (**Fig. 1A+B, S1A, Table S1**).

163 We delineated COVID-19-induced alterations of the major leukocyte lineages by mass cytometry
164 on whole blood samples from COVID-19 patients collected between day 6 and day 13 after
165 disease symptom onset and compared them to age-matched healthy controls. Two antibody
166 staining panels were designed to capture alterations in mononuclear cells (lymphocytes,
167 monocytes and dendritic cells, panel 1), and in the granulocyte compartment (panel 2),
168 respectively (**Table S2**). High-resolution SPADE analysis was performed with 400 target nodes
169 and individual nodes were aggregated into cell subsets according to the expression of lineage-
170 specific cell markers, such as CD14 for monocytes and CD15 for neutrophils (**Fig. S1B**).
171 Visualization of t-distributed stochastic neighbor embedding (tSNE)-automated analysis
172 revealed a clear separation of samples from COVID-19 patients and healthy controls, with marked
173 changes of the monocyte- and the granulocyte compartment (**Fig. 1C**). Comparison of healthy
174 control samples utilized for mass cytometry (HC CyTOF) to MCFC data from our recently
175 published cohorts of healthy controls (HC flow) (Kverneland et al., 2016), demonstrated high
176 similarities in the proportions of granulocytes, lymphocytes, T cells, total monocytes and
177 CD14^{lo}CD16^{hi} 'non-classical' monocytes in whole blood samples from healthy controls,
178 irrespective of the applied methodology (**Fig. 1D**). This allowed us to use the absolute numbers
179 of the published cohorts to also report differences in absolute numbers in COVID-19 samples. In
180 line with recent reports (Barnes et al., 2020; Xintian et al., 2020), we observed a marked
181 leukocytosis with increased proportions of granulocytes and neutrophils in patients with severe
182 COVID-19 (**Fig. 1D**). In contrast, total lymphocyte- and T cell numbers were strongly reduced in
183 all COVID-19 patients. Furthermore, we found a significant reduction of monocytes, particularly
184 non-classical monocytes were virtually absent in COVID-19 (**Fig. 1D**). These changes, increased
185 neutrophils in severe COVID-19 and loss of non-classical monocytes in both mild and severe
186 disease, were validated in cohort 2 by MCFC (**Fig. S1C**).

187
188 Thus, SARS-CoV-2 infection induces lymphopenia and strong alterations within the myeloid
189 compartment, with a drastic reduction of non-classical monocytes and neutrophilia in severe
190 cases of COVID-19.

191

192 **Severity-dependent alterations of the myeloid cell compartment in COVID-19**

193

194 Given the dramatic changes in various immune cell populations in COVID-19 (**Fig. 1C+D**), we
195 next assessed their composition and activation status during the course of SARS-CoV-2 infection
196 by droplet-based scRNA-seq in 21 samples from 12 COVID-19 patients (4 mild & 8 severe, cohort
197 1, **Table S1**) collected between day 7 and day 20 after disease symptom onset. A total of 25,667
198 single-cell transcriptomes of PBMC were analyzed together with 22,418 PBMC from a publicly
199 available control dataset (4 healthy donors). Two-dimensional data representation using Uniform
200 Manifold Approximation and Projection (UMAP) and high-resolution cell type classification
201 identified all major cell types expected in the mononuclear compartment of blood, with a high
202 granularity in the monocyte compartment as indicated by identification of four monocyte subsets
203 (cluster 2, 5, 12, 14) (**Fig. 2A**). The top 10 genes identifying each cluster can be found in **Fig.**
204 **S2A**. Monocytes in cluster 2, 5, and 14 expressed *CD14*, whereas cluster 12 comprised the non-
205 classical monocytes marked by *FCGR3A* (CD16a). Separate visualization of cells in mild and
206 severe cases, revealed highly disease severity-specific clusters (**Fig. 2B**). A distinct subset of the
207 *CD14*⁺ monocytes marked by high expression of interferon (IFN)-stimulated genes (ISG, cluster
208 5), including *ISG15*, *IFI6*, *IFITM3*, or *APOBEC3A* (**Fig. 2C**), was selectively detected in mild
209 COVID-19. The most prominent change in severe COVID-19, however, was the appearance of
210 two cell populations (cluster 9+13, **Fig. 2B**), that were absent in PBMC of patients with mild
211 COVID-19 and healthy donors. Based on published markers, the cell populations were identified
212 as neutrophils and immature neutrophils (**Fig. 2A+B**). The immature neutrophils (cluster 13)
213 expressed *CD24*, *MMP8*, *DEFA3* and *DEFA4*, whereas the identified neutrophil population
214 (cluster 9) was marked by *FCGR3B* (CD16b), *CXCL8* (IL-8) and *CSF3R* (G-CSF receptor)
215 expression (**Fig. 2C**). The fact that these neutrophil clusters migrated with PBMC fractions on a
216 density gradient marked them as low-density neutrophils (LDN).

217

218 In the second cohort, PBMC from 14 COVID-19 patients (7 mild, 7 severe) sampled between days
219 3 and 28 after onset of symptoms, and 2 controls, were collected for single-cell transcriptomic
220 analysis using a microwell-based platform (BD Rhapsody). In total, high-quality single-cell
221 transcriptomes for 93,297 PBMC were assessed and their overall population structure was
222 visualized in two-dimensional space using UMAP (**Fig. 2D**). Data-driven cell type classification
223 based on public reference transcriptome data (Aran et al., 2019) and cluster-specific marker gene
224 expression depicted the presence of all major cell types expected in the PBMC compartment and
225 revealed the appearance of additional clusters and substructures. The top 10 genes specifically
226 expressed in each cluster of the UMAP depicted in **Fig. 2D** are shown in **Fig. S2B**. Similar to
227 cohort 1, samples in cohort 2 also exhibited a prominent plasticity of the monocyte compartment,
228 which could be subclassified into six clusters (**Fig. 2D**, cluster 1, 3, 5, 9, 12). Disease severity-
229 associated changes seen in cohort 1 were also evident in cohort 2 (**Fig. 2E**). The appearance of
230 LDN populations within the isolated PBMC fraction was validated in cohort 2, albeit at lower
231 frequencies. Immature neutrophils and mature neutrophil cell clusters were detected in both
232 cohorts (cluster 13 and 9 in cohort 1, cluster 18 and 13 in cohort 2) and showed a nearly identical
233 marker gene expression profile (**Fig. 2C**). Similar to cohort 1, a prominent shift in subpopulation
234 occupancy was observed in the monocyte clusters, particularly in cluster 3, 5, and 9 (**Fig. 2D+E**).
235 Comparison of the specific marker genes identified for the monocyte-associated subcluster in

236 cohort 1 with those in the corresponding cluster in cohort 2 revealed presence of the inflammatory
237 ISG signature within the monocyte compartment, although it spread across different clusters in
238 cohort 2 (cluster 9, 3, 1, **Fig. 2C**).

239
240 Single-cell transcriptomics of PBMC from COVID-19 patients identified disease-severity
241 dependent cell subsets in the monocyte compartment as well as the appearance of two LDN
242 populations.

243
244
245 **Mild COVID-19 is characterized by HLA-DR⁺ CD11c⁺ monocytes with an IFN signature**

246
247 The monocyte compartment is particularly affected by COVID-19, as seen by mass cytometry
248 revealing a loss of CD14^{lo}CD16^{hi} non-classical monocytes, particularly in mild COVID-19 (**Fig.**
249 **1C+D**). Substantial shifts in monocyte subpopulation structure were also evident by scRNA-seq
250 depending on disease severity (**Fig. 2**). To further dissect phenotypic alterations of the monocyte
251 compartment in SARS-CoV-2 infection, we applied mass cytometry using a panel of 38 antibodies
252 (**Table S2**, panel 1) to whole blood samples from COVID-19 patients with a mild or severe disease
253 course, and corresponding age- and gender-matched healthy controls. Unsupervised cluster
254 analysis using 15 surface antigens as well as the proliferation marker Ki67 separated the myeloid
255 compartment into subpopulations of 'classical', 'intermediate' and 'non-classical' monocytes,
256 myeloid dendritic cells (mDC) and plasmacytoid dendritic cells (pDC) (**Fig. 3A**). The classical
257 monocyte compartment displayed a high level of heterogeneity and separated into two main
258 subclusters. The majority of classical monocytes showed high expression of activation markers
259 CD38, CD95, and CXCR3. Classical monocyte separated into two main subclusters based on
260 high expression of CD62L and Ki67, indicative of proliferative capacity, *versus* high expression of
261 CD226, CD69, HLA-DR and CD11c identifying highly activated, inflammatory cells (**Fig. 3A**).
262 Monocytes from COVID-19 patients were clearly separated from those of healthy controls by
263 viSNE analyses (**Fig. 3B**), mainly based on higher CD226 and CXCR3 expression in COVID-19
264 (**Fig. S3A**). Enhanced CD226 expression on activated monocytes might promote diapedesis
265 through endothelial junctions and tissue infiltration, potentially explaining the relative reduction in
266 overall monocytes in COVID-19 patients (Reymond et al., 2004). Classical monocytes in mild
267 COVID-19 were enriched in HLA-DR^{hi} and CD11c^{hi} populations compared to severe disease and
268 healthy controls (**Fig. S3A**). Thus, the response pattern of peripheral classical monocytes to
269 SARS-CoV-2 infection is associated with disease severity.

270
271 To investigate molecular responses of monocytes to SARS-CoV-2 infection, we extracted clusters
272 2, 5, 12 and 14 from the PBMC dataset of cohort 1 (**Fig. 2A**) for further in-depth analysis.
273 Monocytes in cluster 2 particularly expressed genes found in classical monocytes, such as *VCAN*
274 and *S100A10*, while cells in cluster 14 were characterized by high expression of *ZFP36L2*, and
275 were hence labeled as *ZFP36L2*⁺ monocytes and classical monocytes, respectively (**Fig. 3C**).
276 Cluster 12 was defined as non-classical monocytes by high expression of *FGR3A*, encoding
277 CD16. As outlined before, the remaining cluster 5 (inflammatory monocytes) was characterized
278 by an ISG program, which was further corroborated by gene ontology enrichment analysis
279 (GOEA), assigning this cluster to 'type I interferon signaling pathway' (**Fig. 3D**). In addition,

280 inflammatory (cluster 5) and non-classical monocytes (cluster 12) were also enriched for ‘MHC
281 class II protein complex’ (MHCII), which is concordant with the high expression of *HLA-DRA* and
282 *HLA-DRB1* in these cells (**Fig. 3C, S3B**). Expression of *CD14* indicated that the ISG⁺ cells
283 represent a population of classical monocytes (**Fig. S3B**). Investigation of PBMC revealed that
284 the number of these inflammatory monocytes differed between patients with mild and severe
285 disease courses (**Fig. 2E**). We next investigated this shift in greater detail in cohort 2. The
286 dimensionality reduction and re-clustering of the monocyte space revealed high transcriptional
287 heterogeneity within the monocyte compartment (**Fig. 3E, S3D**). We identified three classical
288 monocyte clusters (cluster 0, 2, and 6), which showed high ISG expression (**Fig. S3C+E**).
289 Interestingly, only cluster 2 cells co-expressed high levels of MHCII molecules (**Fig. S3C**) and
290 were thereby identified as counterparts of the inflammatory monocyte cluster in cohort 1 (**Fig.**
291 **3C**). In contrast, the remaining two ISG⁺ clusters exhibited low levels of *HLA-DRA* and *HLA-DRB1*
292 expression (**Fig. S3D**), and cluster 6 was additionally characterized by platelet-associated genes
293 (*TUBB1*, *PPBP*, and *PF4*) (**Fig. S3E**), indicating that these cells represent platelet-interacting
294 inflammatory monocytes. Intriguingly, a proportion of cluster 0 monocytes expressed pre-
295 maturation markers like *MPO* and *PLAC8* and *IL1R2*, which were recently linked to an immature
296 monocyte population found in sepsis patients (Reyes et al., 2020) (**Fig. S3F**). Indeed, the gene
297 signatures derived from these sepsis-associated monocytes were specifically enriched in clusters
298 0 and 6 (**Fig. S3G**). Low HLA-DR expression and monocyte immaturity result in reduced
299 responsiveness to microbial stimuli (Veglia et al., 2018), which is why cluster 0 cells are referred
300 to as suppressive monocytes. To understand how the identified cell populations in the patients
301 change over time, we next investigated the time-dependent cluster occupancies per patient in
302 cohort 2 (**Fig. 3F**). This analysis clearly showed that the ISG⁺ inflammatory clusters appeared in
303 the early phase of the disease and gradually decreased over time. In addition, the inflammatory
304 cluster 2 was associated with patients exhibiting a mild course of the disease, whereas the
305 suppressive cluster 0 and platelet-activated monocyte cluster 6 were associated with severe
306 disease. The gradual decrease of the ISG⁺ clusters was also evident in cohort 1, which showed
307 a clear time-dependent decrease of *IFI6* and *ISG15* (**Fig. S3H**).

308
309 Taken together, we observed dynamic changes of the monocyte compartment in SARS-CoV-2-
310 infected patients, associated with disease severity and time after onset of disease.

311
312
313 **Low-density neutrophils emerge in severe COVID-19 patients indicative of emergency**
314 **myelopoiesis**

315
316 Surprisingly, PBMC preparations in both cohorts contained two distinct clusters (**Fig. 2A**, clusters
317 9, 13; **Fig. 2D**, clusters 13, 18) of LDN, specifically in patients with severe disease. Since LDN in
318 cohort 1 were more frequent than in cohort 2, we focused our in-depth analysis on cohort 1 data.
319 We subsampled all LDN (**Fig. 4A**) and re-clustered the cells which gave rise to 8 transcriptionally
320 distinct clusters within the LDN compartment of PBMC (**Fig. 4A+B**). We first analyzed previously
321 described markers for pre-neutrophils, immature and mature neutrophils (Ng et al., 2019; Scapini
322 et al., 2016) and identified cluster 4 as CD15(*FUT4*)⁺CD63⁺CD66b(*CEACAM8*)⁺ pre-neutrophils,
323 clusters 3 and 6 as CD11b(*ITGAM*)⁺CD101⁺ immature neutrophils and the remaining clusters as

324 mature neutrophils (**Fig. S4A**). The identification of pre-neutrophils and immature neutrophils was
325 further supported by signature enrichment of neutrophil progenitors derived from previous single-
326 cell data (**Fig. 4C**) (Pellin et al., 2019; Popescu et al., 2019). Cell cycle gene analysis further
327 corroborated cluster 4 being pre-neutrophils with the highest proportion of cells per cluster
328 showing a proliferative signature (**Fig. S4B**). Clusters 0, 1, 2 and 5 (originally from cluster 9 in **Fig.**
329 **2A**) were characterized by expression of the mature neutrophil markers *FCGR3A* (CD16) and
330 *MME* (CD10) (**Fig. S4A**).

331
332 Visualizing the most differentially expressed genes for each cluster revealed extensive phenotypic
333 heterogeneity within the LDN compartment (**Fig. 4B**). For example, cluster 5 (ISG⁺ neutrophils)
334 within the mature neutrophils highly expressed many ISGs (*ISG15*, *IFITM1/3* and *RSAD2*),
335 strongly supporting an activated inflammatory neutrophil phenotype. Cluster 4 (pre-neutrophils)
336 expressed several genes (e.g. *MPO*, *ELANE*, *PRTN3*) that have been associated with
337 pathophysiological conditions including sepsis (Ahmad et al., 2019; Carbon et al., 2019; Silvestre-
338 Roig et al., 2019). Similarly, immature neutrophils (clusters 3 and 6) expressed other genes (e.g.
339 *CD24*, *LCN2*) previously associated with unfavorable outcome in sepsis (Kangelaris et al., 2015).

340
341 LDN mainly arise under pathological conditions, notably in infection and sepsis in the context of
342 emergency myelopoiesis, and they have been associated with dysfunctional immune responses
343 marked by combined immunosuppression and inflammation (Silvestre-Roig et al., 2019). We
344 therefore investigated the expression of prominent genes previously linked to such pathological
345 conditions (**Fig. 4D+E**). Pre-neutrophils strongly expressed *PRTN3*, *ELANE*, and *MPO*, genes
346 that are involved in neutrophil extracellular trap formation (Stiel et al., 2018; Thomas et al., 2014;
347 You et al., 2019) among other functions. Both pre-neutrophils and immature neutrophils
348 expressed *PADI4*, another co-factor in NETosis (Leshner et al., 2012). NETs have recently been
349 implicated in the pathogenesis of COVID-19 (Barnes et al., 2020; Zuo et al., 2020). Other genes,
350 including *CD24*, *Olfactomedin* (*OLFM4*), *Lipocalin 2* (*LCN2*), Bactericidal/permeability-increasing
351 protein (*BPI*), previously associated with poor outcome in sepsis, were highly expressed in pre-
352 and immature neutrophils (Kangelaris et al., 2015). We also observed a very strong expression
353 of the alarmins *S100A8* and *S100A9*, which is not restricted to the pre-and immature state (**Fig.**
354 **4D**). Other members of the S100 gene family (e.g. *S100A4*, *S100A12*) are also strongly induced
355 in different neutrophil clusters. Finally, known inhibitors of T cell activation, namely *PD-L1*
356 (*CD274*) and *Arginase 1* (*ARG1*) (Bronte et al., 2003; Li et al., 2018) were highly expressed in
357 neutrophils in COVID-19 patients (**Fig. 4E**). *PD-L1*⁺ mature neutrophils (clusters 0, 5) resemble
358 cells found in HIV-1 infected patients (Bowers et al., 2014). *ARG1*⁺ cells were found among
359 mature and immature neutrophils (clusters 1, 2, 3, 4 and 6) and did not overlap with *PD-L1*
360 expression suggesting an emergence of different populations of suppressive neutrophils in
361 COVID-19. *ARG1*⁺ neutrophils in sepsis patients were shown to deplete arginine and constrain T
362 cell function in septic shock (Darcy et al., 2014), and were predictive of the development of
363 nosocomial infections (Uhel et al., 2017). Collectively, analyzing the LDN compartment recovered
364 from PBMC fractions of COVID-19 patients revealed multiple mechanisms that might contribute
365 to severe disease course and dysregulated immune responses.

366
367

368 **Persistent increase in activated and immunosuppressive neutrophils in severe COVID-19**

369

370 To further dissect the profound alterations within the neutrophil compartment, we applied mass
371 cytometry to whole blood samples from cohort 1 and age- and gender-matched healthy controls.
372 We specifically designed the antibody panel 2 to not only identify neutrophils but also discriminate
373 between maturation stages and reveal phenotypical signs of activation, immunosuppressive
374 properties or dysfunction. Unsupervised clustering analysis of all neutrophils acquired from
375 healthy control and COVID-19 samples identified 7 major subsets (**Fig. 5A**). Whereas neutrophils
376 belonging to cell subsets 2, 5 and 7 appeared quiescent, with low expression of activation markers
377 like CD64, neutrophil subsets 1 and 6 appeared to be dominated by highly activated, CD64⁺,
378 Siglec 8⁺, RANK⁺ and RANKL⁺ as well as Ki67⁺ proliferating cells. Cells within subset 3 adopted
379 an intermediate phenotype. Neutrophils from COVID-19 patients clearly separated from those of
380 healthy controls, and neutrophils in patients with severe COVID-19 were distinct from those of
381 patients with mild disease (**Fig. 5B**). Subset 1 was highly enriched for neutrophils from COVID-
382 19 patients. Consequently, we observed an increase in CD34⁺ immature and activated neutrophils
383 with high CD64, Siglec 8, RANK and RANKL (Riegel et al., 2012) expression in samples from
384 COVID-19 patients regardless of disease course (**Fig. 5B+C**). In contrast, CD62L was exclusively
385 downregulated in up to 50% of the neutrophils from severe but not mild COVID-19 patients,
386 indicative of distinct dysfunctional neutrophil populations with immunosuppressive properties
387 (Kamp et al., 2012; Pillay et al., 2012; Tak et al., 2017). These findings were further supported by
388 upregulation of CD123 and PD-L1 expression (**Fig. 5B+C**) as hallmarks of myeloid-derived
389 suppressor cell (MDSC) function (Cassetta et al., 2019; Testa et al., 2004; Younos et al., 2015)
390 on neutrophils of severe COVID-19 patients. In addition, neutrophils of severe COVID-19 patients
391 adopted an aged phenotype with elevated CD45 expression (**Fig. 5B**).

392

393 Thus, SARS-CoV-2 infection induces major alterations in the neutrophil compartment. While
394 neutrophils in patients with mild COVID-19 display an activated phenotype, additional markers of
395 immunosuppression or dysfunction are upregulated in patients with severe disease.

396

397 The differences in the functional states of neutrophils in mild and severe COVID-19 in the snap-
398 shot analysis, prompted us to perform a longitudinal analysis. We analyzed samples according to
399 collection either within the first 10 days (early) or during the second and third week (late) after
400 onset of disease symptoms. The proportional increase in total granulocytes and CD34⁺ neutrophil
401 subset in severe COVID-19 was only detected during the early phase of the disease (**Fig. 5D+E**).
402 However, the additionally observed alterations in the neutrophil compartment such as loss of
403 CD62L expression accompanied by increase of CD123 and PD-L1 positive populations as signs
404 of dysfunctionality and immunosuppressive properties were persistent in severe COVID-19
405 patients (**Fig. 5E**).

406

407 Next, we analyzed whether similar to the evolution on the transcriptional level, we can also capture
408 time-dependent changes of the monocyte compartment on the protein level. The proportion of
409 non-classical monocytes started to recover in mild patients during the later stages of the disease
410 (**Fig. 5D**). This was accompanied by reduced CD11c and CXCR3 expression in classical
411 monocytes (**Fig. 5F**) and relates very well to the described longitudinal changes of the HLA-DR

412 & ISG⁺ monocyte cluster (**Fig. 3F, S3H**). In contrast, although classical monocytes of severe
413 patients never showed high CD11c expression, they maintained high levels of CXCR3 expression
414 even in late stages of the disease, indicating prolonged activation (**Fig. 5F**). Thus, severe COVID-
415 19 patients are characterized by a combination of persistent inflammation and
416 immunosuppression, which is reminiscent of long-term post-traumatic complications (Hesselink
417 et al., 2019). Our data reveal an early strong monocyte activation versus persistent signs of
418 neutrophil dysfunctionality as discriminators between mild and severe COVID-19.

419
420

421 **Single cell transcriptomes of whole blood neutrophils reveal suppressive signatures in** 422 **severe COVID-19**

423

424 Whole blood CyTOF analysis (cohort 1) clearly indicated a very distinct molecular regulation
425 within the neutrophil compartment in severe and mild COVID-19. To further delineate this
426 regulation with respect to the underlying transcriptional programs, we performed scRNA-seq
427 analysis on fresh whole blood samples from 19 individuals (21 samples, cohort 2). Overlay of all
428 samples of cohort 2 (fresh/frozen PBMC, fresh whole blood, 162,697 cells, **Fig. S6A**), without
429 batch correction, revealed the major cell type distribution, including the granulocyte compartment
430 (**Fig. 6A, S6A**). Cell type distribution as identified by scRNA-seq (**Fig. S6B**) strongly correlated
431 with the MCFC data of the same samples (**Fig. S6C**). We noticed abnormal transcriptional
432 activation in six samples, which was caused by protracted cold treatment (4°C) prior to single-cell
433 sampling, as recently described for PBMC (Massoni-Badosa et al., 2020). These samples were
434 therefore excluded from further analysis. The remaining 30,019 neutrophils were subsampled and
435 revealed a structure of 11 clusters (**Fig. 6B-C**). Using marker- and data-driven approaches as
436 applied to LDN (**Fig. 4D, S4A**), we identified CD15(*FUT4*)⁺CD63⁺CD66b⁺CD101⁺CD10⁻ pre-
437 neutrophils, CD11b(*ITGAM*)⁺CD101⁺CD10⁻ immature neutrophils along with 9 mature neutrophil
438 clusters (**Fig. 6B-D, S6D-E**). Heterogeneous expression of various markers involved in neutrophil
439 function including *SELL* (L-selectin, CD62L), *CXCR2*, *FCGR2* (CD32), and *CD10* as a marker for
440 mature neutrophils, pointed towards distinct functionalities within the neutrophil compartment
441 (**Fig. 6C, 6H, S6E**). The phenotypic diversity was further corroborated, when we assessed the
442 expression of markers previously identified by CyTOF to be differentially regulated in patients with
443 severe COVID-19 (**Fig. 5**). For example, we found elevated expression of *CD274* (PD-L1) and
444 *CD64* in neutrophil clusters identified specifically in patients with severe COVID-19 (**Fig. 6E, S6F**).
445 Out of the 11 neutrophil clusters identified in whole blood in cohort 2, 10 clusters could also be
446 mapped to fresh PBMC samples in cohort 1 (**Fig. S6D**), indicating that scRNA-seq of fresh PBMC
447 - in COVID-19 patients - reveals relevant parts of the neutrophil compartment. When we analyzed
448 PBMC samples of cohort 2, these clusters could be identified in fresh samples, but were lost upon
449 freezing (**Fig. S6A**). Importantly, the analysis corroborated the transcriptional phenotype of pre-
450 neutrophils and immature neutrophils (cluster 8+9) in cohort 2 (**Fig. 6B-D, S6D-E**).

451 Heatmap and UMAP visualization of the cell type distribution identified pre-neutrophils and
452 immature neutrophils in severe COVID-19, at late time points (**Fig. 6F-G**). Furthermore, clusters
453 2 and 0 were associated with severe COVID-19, while clusters 5 and 10 were found in mild
454 COVID-19 (**Fig. 6F-G**). IFN-signatures were detected in neutrophils from mild and severe COVID-
455 19 patients and even in some of the clusters derived from controls (**Fig. S6G**). However,

456 expression of *CD177*, *CD274* (PD-L1) and zinc finger DHHC domain-containing palmitoyl
457 transferases *ZDHHC19*, indicative of an immature and suppressive granulocyte phenotype
458 (Volkman et al., 2020), was specifically observed in patients with severe COVID-19 (**Fig. 6C**).
459 *ZDHHC19* has been shown to promote palmitoylation of STAT3 (Niu et al., 2019), as well as the
460 Chikungunya virus derived protein nsP1 (Zhang et al., 2018). In addition, neutrophils in severe
461 COVID-19 expressed *FCGR1A*, *ICAM1* and *ZC3H12A* (**Fig. 6H**), indicative of their suppressive
462 nature. As indicated by the clustering in the UMAP (**Fig. 6B+G**), pseudotime analysis strongly
463 suggested that cells in cluster 2 preceded those in cluster 0, and particularly *CD274* (PD-1L) was
464 among the genes that further enriched in cluster 0 compared to cluster 2, indicating a progression
465 towards a suppressive phenotype in late stage disease (**Fig. S6H+I**). Predictions of transcription
466 factor (TF)-based regulation of the cluster-specific gene signatures revealed a strict separation of
467 mature neutrophils from pre-neutrophils and immature neutrophils (**Fig. S6J**), but showed a
468 surprisingly high overlap between clusters 5 (mild), 2 (severe early), and 0 (severe late) in STAT-
469 and IRF-family member TFs (**Fig. 6I**). However, there was a striking loss of important TF hubs in
470 cluster 0, found in late stage severe COVID-19 (**Fig. 6I**).

471
472 Collectively, the neutrophil compartment in peripheral blood of COVID-19 patients is
473 characterized by the appearance of LDN, *ARG1⁺MPO⁺BPI⁺* pre-neutrophils and *CD10⁺*
474 *S100A8/A9⁺* immature neutrophils, reminiscent of emergency myelopoiesis, as well as
475 *CD274⁺*(PD-L1⁺) suppressive mature neutrophils. All neutrophil subsets emerging in severe
476 COVID-19 express an armamentarium of genes associated with suppressive functions as they
477 have been described for sepsis or ARDS, indicating that a dysregulated myeloid cell compartment
478 contributes to severe COVID-19.

479

480 Discussion

481
482 SARS-CoV-2 infection generally causes mild disease in the majority of individuals, however about
483 10-20% of COVID-19 patients progress to severe disease with pneumonia and respiratory failure.
484 The case-fatality ratio was found to be 49% among patients with critical illness and respiratory
485 failure (Wu and McGoogan, 2020). The pathomechanisms that govern progression from mild
486 COVID-19 to potentially fatal courses of disease are currently unknown, but dysregulated immune
487 responses have been repeatedly described in patients with severe COVID-19 (Zhou et al., 2020c).
488 Detailed knowledge of the underlying molecular processes is urgently needed in order to identify
489 predictive biomarkers and therapeutic targets for severe COVID-19, which could enable
490 individualized treatments.

491
492 Here, we employed five complementary technologies at single-cell resolution to assess
493 differences in the systemic immune response in patients with mild or severe courses of COVID-
494 19. We analyzed a total of 131 samples from two independent cohorts collected at two university
495 medical centers in Germany. The combination of single-cell transcriptomics and single-cell
496 proteomics, using different technological platforms and sample-processing strategies in
497 independent patient cohorts provided unprecedented insights into the systemic immune
498 responses in COVID-19 and allowed for cross-validation of key findings.

499
500 This multipronged approach revealed drastic changes within the myeloid cell compartment,
501 particularly in patients with a severe course of disease. Early activation of HLA-DR^{hi}CD11c^{hi}
502 monocytes with a strong antiviral IFN-signature was a hallmark of mild COVID-19, which receded
503 during the natural course of disease, as demonstrated at later time points in patients with mild
504 COVID-19. In contrast, we found clear evidence of emergency myelopoiesis with release of pre-
505 neutrophils and immature neutrophils with immunosuppressive features in severe COVID-19.
506 Prolonged partial monocyte activation and release of dysfunctional neutrophils may thus
507 contribute to severe disease course and ARDS development.

508
509 Several reports have described inflammatory monocyte responses, with a strong IFN-signature
510 in COVID-19 (Liao et al., 2020; Merad and Martin, 2020; Zhou et al., 2020c). Mononuclear
511 phagocytes and neutrophils appear to dominate inflammatory infiltrates in the lungs, and resident
512 alveolar macrophages are replaced by inflammatory monocyte-derived macrophages in patients
513 with severe COVID-19 (Liao et al., 2020). Here, we report substantial alterations of the monocyte
514 compartment, with time- and disease severity-dependent changes in two separate cohorts of
515 COVID-19 patients. We observed a depletion of CD14^{lo}CD16^{hi} non-classical monocytes in all
516 patients, which was particularly prominent in mild cases and less pronounced in severe disease
517 (**Fig. 1D**). This is in line with previous reports, and it has also been observed in other severe viral
518 infections (Lüdtke et al., 2016; Naranjo-Gómez et al., 2019). Strikingly, we found a strong transient
519 increase in highly activated CD14⁺CD11c^{hi}HLA-DR^{hi} ISG⁺ monocytes in mild cases of COVID-19,
520 which were absent in severe cases (**Fig. 3**). In contrast, we identified immature suppressive
521 monocytes with low expression of HLA-DR in patients with severe disease. Low HLA-DR
522 expression on monocytes has been previously associated with an increased risk to develop

523 infectious complications after trauma (Hoffmann et al., 2017) and increased mortality in septic
524 shock (Monneret et al., 2006). Furthermore, CD14⁺HLA-DR^{lo/neg} monocytes, have also been
525 identified as important mediators of tumor-induced immunosuppression (Mengos et al., 2019).
526 Indeed, the severe COVID-19-specific immunosuppressive monocyte cluster showed enrichment
527 of genes previously identified in sepsis patients (**Fig. S3H**) (Reyes et al., 2020).

528
529 Acute pathological insults, such as trauma or severe infections, trigger a process referred to as
530 emergency myelopoiesis in order to replenish functional granulocytes and other hematopoietic
531 cells. Emergency myelopoiesis is characterized by the mobilization of immature myeloid cells,
532 which exert immunosuppressive functions (Loftus et al., 2018; Schultze et al., 2019). Emergence
533 of suppressive myeloid cells has been previously observed during sepsis and severe influenza
534 virus infection (Darcy et al., 2014; Loftus et al., 2018; Sander et al., 2010; De Santo et al., 2008).
535 Here we detected pre-neutrophils and immature neutrophils within PBMC, indicating their reduced
536 cellular density, specifically in severe COVID-19 (**Fig. 4**). These LDN showed an immature gene
537 expression profile and a surface marker and gene expression profile indicative of
538 immunosuppressive functions. For example, olfactomedin-4⁺ LDN have been associated with
539 immunopathogenesis in sepsis (Alder et al., 2017).

540
541 Suppressive neutrophils have been shown to increase in patients with bacterial sepsis and their
542 frequencies correlated with sepsis severity and systemic inflammation (Darcy et al., 2014), as well
543 as in healthy volunteers treated with G-CSF (Hartung et al., 1995). Analyzing whole blood
544 samples without density separation, we identified neutrophils with an IFN-signature in mild and
545 severe COVID-19, but only in patients with severe disease, these activated neutrophils also
546 expressed PD-L1 (*CD274*), which further increased in expression in late stage disease. The
547 expression of *CD177* on mature activated neutrophils at early stages, but not at later stages, and
548 the identification of genes associated with suppressive cellular functions (*ZDHHC19*, *ZC3H12A*)
549 strongly favor a model in which neutrophils emerging prematurely from the bone marrow are
550 programmed towards a suppressive program in severe COVID-19. The transcriptional programs
551 induced in pre-neutrophils, immature and mature COVID-19-associated neutrophil clusters may
552 also align with other clinical observations in severe COVID-19 patients, including increased NET
553 formation (Barnes et al., 2020; Zuo et al., 2020), coagulation (Klok et al., 2020; Pfeiler et al., 2014)
554 and immunothrombosis (Stiel et al., 2018; Xu et al., 2020). In contrast, in patients with mild
555 COVID-19, none of these transcriptional programs was observed. Despite the fact that SARS-
556 CoV2^{neg} controls exhibited a range of comorbidities (e.g. COPD, type diabetes II), we did not
557 observe this massive expansion of suppressive neutrophils in these chronic inflammatory
558 conditions. The pathophysiological consequences of this suppressive signature in severe COVID-
559 19 are unclear at this stage, but it is highly likely that they contribute to immunoparalysis in
560 critically ill patients, potentially leading to insufficient host defense, disbalanced inflammation and
561 increased susceptibility to superinfections.

562
563 Collectively, our data link a striking appearance of immature and suppressive cells, in both the
564 monocyte and neutrophil compartment, to disease severity in COVID-19. Consequently, for the
565 development of better treatments and prevention of severe COVID-19, we may benefit from

566 achievements in other fields such as cancer, which have successfully applied therapies targeting
567 suppressive myeloid cells.

568 STAR Methods

569 Study subjects

570 *Cohort 1 / Berlin cohort*

571 This study includes a subset of patients enrolled between March 2 and March 27 2020 in the Pa-
572 COVID-19 study, a prospective observational cohort study assessing pathophysiology and clinical
573 characteristics of patients with COVID-19 at Charité Universitätsmedizin Berlin (Kurth et al.,
574 2020). The study is approved by the Institutional Review board of Charité (EA2/066/20). Written
575 informed consent was provided by all patients or legal representatives for participation in the
576 study. The patient subset included in this analysis contains 7 healthy donors (**Table S1**) and 19
577 COVID-19 patients (**Figure 1A+B, Table S1**). All COVID-19 patients tested positive for SARS-
578 CoV-2 RNA in nasopharyngeal swabs.

579 *Cohort 2 / Bonn cohort*

580 This study was approved by the Institutional Review board of the University Hospital Bonn (073/19
581 and 134/20). After providing written informed consent, 12 control donors (**Table S1**) and 14
582 COVID-19 patients (**Figure 1A+B, Table S1**) were included in the study. In patients who were
583 not able to consent at the time of study enrollment, consent was obtained after recovery. COVID-
584 19 patients who tested positive for SARS-CoV-2 RNA in nasopharyngeal swabs were recruited
585 at the Medical Clinic I of the University Hospital Bonn between March 30 and May 17, 2020.

586

587 Isolation of blood cells for scRNA-seq

588 *Cohort 1 / Berlin cohort*

589
590 PBMC were isolated from heparinized whole blood by density centrifugation over Pancoll (density:
591 1.077g/ml; PAN-Biotech™). If the pellet was still slightly red, remaining CD235ab⁺ cells
592 (Erythrocytes) were depleted by Negative Selection (*MagniSort*™ Thermo Fisher). Subsequently
593 the PBMC were prepared for 3'scRNA-seq (10xGenomics) or cryopreserved and analyzed later.
594

595 *Cohort 2 / Bonn cohort*

596 In the Bonn cohort, scRNA-seq was performed on fresh whole blood, fresh PBMC and frozen
597 PBMC. Briefly, PBMC were isolated from EDTA-treated or heparinized peripheral blood by density
598 centrifugation over Pancoll or Ficoll-Paque density centrifugation (density: 1.077g/ml). Cells were
599 then washed with DPBS, directly prepared for scRNA-seq (BD Rhapsody) or cryopreserved in
600 RPMI-1640 with 40% FBS and 10% DMSO. Whole blood was prepared by treatment of 1 ml
601 peripheral blood with 10 ml of RBC lysis buffer (Biolegend). After one wash in DPBS cells were
602 directly processed for scRNA-seq (BD Rhapsody) or MCFC. Frozen PCMC were recovered by

603 rapidly thawing frozen cell suspensions in a 37° C water bath followed by immediate dilution in
604 pre-warmed RPMI-1640+10% FBS (Gibco) and centrifugation at 300g for 5 min. After
605 centrifugation, the cells were resuspended in RPMI-1640+10% FBS and processed for scRNA-
606 seq. Antibody cocktails were cryopreserved as described before (Schulz et al., 2019).

607 **Antibodies used for mass cytometry**

608
609 All anti-human antibodies pre-conjugated to metal isotopes were obtained from Fluidigm
610 Corporation (San Francisco, US). All remaining antibodies were obtained from the indicated
611 companies as purified antibodies and in-house conjugation was done using the MaxPar X8
612 labeling kit (Fluidigm). Supplementary table 2 shows a detailed list of all antibodies used for panel
613 1 and panel 2.

615 **Sample processing, antigen staining and data analysis of mass cytometry-based immune 616 cell profiling**

617
618 500 µl of whole blood (heparin) was fixed in 700 µl of proteomic stabilizer (Smart Tube Inc., San
619 Carlos, US) as described in the user manual and stored at -80°C until further processing. Whole
620 blood samples were thawed in Thaw/Lyse buffer (Smart Tube Inc.). For barcoding antibodies
621 recognising human beta-2 microglobulin (B2M) were conjugated in house to ¹⁰⁴Pd, ¹⁰⁶Pd, ¹⁰⁸Pd,
622 ¹¹⁰Pd, ¹⁹⁸Pt (Mei et al., 2015, 2016; Schulz and Mei, 2019). Up to 10 individual samples were
623 stained using a staining buffer from Fluidigm with a combination of two different B2M antibodies
624 for 30 min at 4°C. Cells were washed and pooled for surface and intracellular staining.

625 For surface staining the barcoded and pooled samples were equally divided into two samples.
626 Cells were resuspended in antibody staining cocktails for panel 1 or panel 2 respectively (**Table**
627 **S2**) and stained for 30 min at 4°C. For secondary antibody staining of panel 2, cells were washed
628 and stained with anti-APC ¹⁶³Dy for 30 min at 4°C. After surface staining cells were washed with
629 PBS, resuspended in cell-ID intercalator ¹⁰³Rh to discriminate between live and dead cells and
630 incubated for 5 min at room temperature. After washing, cells were fixed overnight in 2 % PFA
631 solution diluted dissolved in PBS to 2%.

632 For intracellular staining cells were washed twice with a permeabilization buffer (eBioscience, San
633 Diego, US) and stained with the respective antibodies diluted in a permeabilization buffer for 30
634 min at room temperature. After washing, cells were stained with iridium intercalator (Fluidigm)
635 diluted in 2 % PFA for 20 min at room temperature. Cells were washed once with PBS and then
636 twice with ddH₂O and kept at 4°C until mass cytometry measurement.

637 A minimum of 100.000 cells per sample and panel were acquired on a CyTOF2/Helios mass
638 cytometer (Fluidigm). For normalization of the fcs files 1:10 EQ Four Element Calibration Beads
639 (Fluidigm) were added. Cells were analyzed using a CyTOF2 upgraded to Helios specifications,
640 with software version 6.7.1014, using a narrow bore injector. The instrument was tuned according
641 to the manufacturer's instructions with tuning solution (Fluidigm) and measurement of EQ four
642 element calibration beads (Fluidigm) containing 140/142Ce, 151/153Eu, 165Ho and 175/176Lu
643 served as a quality control for sensitivity and recovery. Directly prior to analysis, cells were
644 resuspended in ddH₂O, filtered through a 20-µm cell strainer (Celltrics, Sysmex), counted and
645 adjusted to 5-8 x 10⁵ cells/ml. EQ four element calibration beads were added at a final

646 concentration of 1:10 v/v of the sample volume to be able to normalize the data to compensate
647 for signal drift and day-to-day changes in instrument sensitivity. Samples were acquired with a
648 flow rate of 300-400 events/s. The lower convolution threshold was set to 400, with noise
649 reduction mode turned on and cell definition parameters set at event duration of 10-150 pushes
650 (push = 13 μ s). The resulting flow cytometry standard (FCS) files were normalized and
651 randomized using the CyTOF software's internal FCS-Processing module on the non-randomized
652 ('original') data. The default settings in the software were used with time interval normalization
653 (100 s/minimum of 50 beads) and passport version 2. Intervals with less than 50 beads per 100
654 s were excluded from the resulting FCS file.

655 **Blood processing for flow cytometry**

656
657 1 ml of fresh blood from control or COVID-19 donors was treated with 10 ml of RBC lysis buffer
658 (Biolegend). After RBC lysis, cells were washed with DPBS and 1-2 million cells were used for
659 flow cytometry analysis. Cells were then stained for surface markers (**Table S3**) in DPBS with BD
660 Horizon Brilliant™ Stain Buffer (Becton Dickinson) for 30 min at 4°C. To distinguish live from dead
661 cells, the cells were incubated with LIVE/DEAD Fixable Yellow Dead Cell Stain Kit (1:1000 –
662 Thermo Scientific). Following staining and washing, the cell suspension was fixed with 4% PFA
663 for 5 min at room temperature to prevent any possible risk of contamination during acquisition of
664 the samples. Flow cytometry analysis was performed on a BD Symphony instrument (Becton
665 Dickinson) configured with 5 lasers (UV, violet, blue, yellow-green, red).

666 **10x Genomics Chromium single-cell RNA-seq**

667
668 PBMC were isolated and prepared as described above. Afterwards, patient samples were
669 hashtagged with TotalSeq-A antibodies (Biolegend) according to the manufacturer's protocol for
670 TotalSeq™-A antibodies and cell hashing with 10x Single Cell 3' Reagent Kit v3.1. 50 μ L cell
671 suspension with 1×10^6 cells were resuspended in staining buffer (2% BSA, Jackson Immuno
672 Research; 0,01% Tween-20, Sigma-Aldrich; 1x DPBS, Gibco) and 5 μ L Human TruStain FcX™
673 FcBlocking (Biolegend) reagent were added. The blocking was performed for 10 min at 4°C. In
674 the next step 1 μ g unique TotalSeq-A antibody was added to each sample and incubated for 30
675 minutes at 4°C. After the incubation time 1.5 mL staining buffer were added and centrifuged for 5
676 minutes at 350g and 4°C. Washing was repeated for a total of 3 washes. Subsequently, the cells
677 were resuspended in an appropriate volume of 1x DPBS (Gibco), passed through a 40 μ m mesh
678 (Flowmi™ Cell Strainer, Merck) and counted, using a Neubauer counting (Marienfeld). Cell counts
679 were adjusted and hashtagged cells were pooled equally. The cell suspension was super-loaded,
680 with 50,000 cells, in the Chromium™ Controller for partitioning single cells into nanoliter-scale Gel
681 Bead-In-Emulsions (GEMs). Single Cell 3' reagent kit v3.1 was used for reverse transcription,
682 cDNA amplification and library construction of the gene expression libraries (10x Genomics)
683 following the detailed protocol provided by 10xGenomics. Hashtag libraries were prepared
684 according to the cell hashing protocol for 10x Single Cell 3' Reagent Kit v3.1 provided by
685 Biolegend, including primer sequences and reagent specifications. Biometra Trio Thermal Cycler
686 was used for amplification and incubation steps (Analytik Jena). Libraries were quantified by
687 Qubit™ 2.0 Fluorometer (ThermoFisher) and quality was checked using 2100 Bioanalyzer with

688 High Sensitivity DNA kit (Agilent). Sequencing was performed in paired-end mode with a S1 and
689 S2 flow cell (2 × 50 cycles kit) using NovaSeq 6000 sequencer (Illumina).

690 **BD Rhapsody single-cell RNA-seq**

691
692 Whole transcriptome analyses, using the BD Rhapsody Single-Cell Analysis System (BD,
693 Biosciences) were performed on PBMC and whole blood samples prepared as described above.
694 Cells from each sample were labeled with sample tags (BD™ Human Single-Cell Multiplexing Kit)
695 following the manufacturer's protocol. Briefly, a total number of 1×10^6 cells were resuspended in
696 180µl of Stain Buffer (FBS) (BD Pharmingen). The sample tags were added to the respective
697 samples and incubated for 20 min at room temperature. After incubation, 200µl stain buffer was
698 added to each sample and centrifuged for 5 minutes at 300g and 4°C. Samples were washed one
699 more time. Subsequently cells were resuspended in 300µl of cold BD Sample Buffer and counted
700 using Improved Neubauer Hemocytometer (INCYTO). Labelled samples were pooled equally in
701 650µl cold BD Sample Buffer. For each pooled sample two BD Rhapsody cartridges were super-
702 loaded with approximately 60,000 cells each. Single cells were isolated using Single-Cell Capture
703 and cDNA Synthesis with the BD Rhapsody Express Single-Cell Analysis System according to
704 the manufacturer's recommendations (BD Biosciences). cDNA libraries were prepared using the
705 BD Rhapsody™ Whole Transcriptome Analysis Amplification Kit following the BD Rhapsody™
706 System mRNA Whole Transcriptome Analysis (WTA) and Sample Tag Library Preparation
707 Protocol (BD Biosciences). The final libraries were quantified using a Qubit Fluorometer with the
708 Qubit dsDNA HS Kit (ThermoFisher) and the size-distribution was measured using the Agilent
709 high sensitivity D5000 assay on a TapeStation 4200 system (Agilent technologies). Sequencing
710 was performed in paired-end mode (2*75 cycles) on a NovaSeq 6000 and NextSeq 500 System
711 (Illumina) with NovaSeq 6000 S2 Reagent Kit (200 cycles) and NextSeq 500/550 High Output Kit
712 v2.5 (150 Cycles) chemistry, respectively.

713

714 **Data pre-processing of 10x Genomics Chromium scRNA-seq data**

715

716 CellRanger v3.1.0 (10x Genomics) was used to process scRNA-seq. To generate a digital gene
717 expression (DGE) matrix for each sample, we mapped their reads to a combined reference of
718 GRCh38 genome and SARS-CoV-2 genome, and recorded the number of UMIs for each gene in
719 each cell.

720

721 **Data pre-processing of BD Rhapsody scRNA-seq data**

722

723 After demultiplexing of bcl files using Bcl2fastq2 V2.20 from Illumina and quality control, paired-
724 end scRNA-seq reads were filtered for valid cell barcodes using the barcode whitelist provided by
725 BD. Cutadapt 1.16 was then used to trim NexteraPE-PE adapter sequences where needed and
726 to filter reads for a PHRED score of 20 or above. Then, STAR 2.6.1b was used for alignment
727 against the Gencode v33 (GRCh38.p13) reference genome. dropseq-tools 2.0.0 were used to
728 quantify gene expression and collapse to UMI count data. For hashtag-oligo based demultiplexing
729 of single-cell transcriptomes and subsequent assignment of cell barcodes to their sample of origin

730 the respective multiplexing tag sequences were added to the reference genome and quantified
731 as well.

732

733 **ScRNA-seq data analysis of 10x Chromium data of cohort 1**

734

735 ScRNA-seq UMI count matrices were imported to R 3.6.2 and gene expression data analysis was
736 performed using the R/Seurat package 3.1.4 (Butler et al., 2018; Hafemeister and Satija, 2019).
737 Demultiplexing of cells was performed using the *HTODemux* function implemented in Seurat.

738

739 ***Data quality control.***

740 We excluded the cells based on the following criteria: more than 5% mitochondrial reads, less
741 than 200 expressed genes or more than 6000 expressed genes. We further excluded genes that
742 were expressed in less than five cells. In addition, mitochondrial genes have been excluded from
743 further analysis.

744

745 ***Data integration.***

746 First, we SCTransformed (Seurat function) the data and then selected 2,000 features with largest
747 variance among the data sets and identified integration anchors using these features. PCA
748 (principal component analysis) was then performed on the integrated data sets, followed by a
749 Shared Nearest Neighbour (SNN) Graph construction using PC1 to PC30 and for the k-Nearest
750 Neighbours (KNN) Graph construction. The clustering analysis was performed using the Louvain
751 algorithm with a resolution of 0.6. Uniform Manifold Approximation and Projection (UMAP) was
752 utilized to visualize the cell clusters.

753 Data of control (healthy) samples were obtained from <https://satijalab.org/seurat/vignettes.html>
754 and <https://support.10xgenomics.com/single-cell-gene-expression/datasets/1.1.0/>.

755

756 ***Normalization.***

757 LogNormalization (Seurat function) was applied before downstream analysis. The original gene
758 counts for each cell were normalized by total UMI counts, multiplied by 10,000 (TP10K) and then
759 log transformed by $\log_{10}(\text{TP10k}+1)$.

760

761 ***Differential expression tests and cluster marker genes.***

762 Differential expression (DE) tests were performed using FindMarkers/FindAllMarkers functions in
763 Seurat with Wilcoxon Rank Sum test. Genes with >0.25 log-fold changes, at least 25% expressed
764 in tested groups, and Bonferroni-corrected p-values <0.05 were regarded as significantly
765 differentially expressed genes (DEGs). Cluster marker genes were identified by applying the DE
766 tests for upregulated genes between cells in one cluster to all other clusters in the dataset. Top
767 ranked genes (by log-fold changes) from each cluster of interest were extracted for further
768 illustration.

769

770 ***Cluster annotation.***

771 Clusters were annotated based on a double-checking strategy: 1) by comparing cluster marker
772 genes with public sources, and 2) by directly visualizing the expression pattern of CyTOF marker
773 genes.

774 ***GO enrichment analysis.***

775 Significantly differentially expressed genes (DEGs) between each monocyte cluster and the rest
776 of monocyte subpopulations were identified by FindMarkers function from the Seurat package
777 using Wilcoxon Rank Sum test statistics for genes expressed in at least 25% of all monocyte
778 clusters. P-values were corrected for multiple testing using Bonferroni correction and genes with
779 corrected P-values lower or equal 0.05 have been taken as significant DEGs for GO enrichment
780 test by R package/ClusterProfiler v.3.10.1 (Yu et al., 2012).

781

782 ***Subset analysis of the neutrophils within the PBMC data set of cohort 1***

783 The neutrophil space was investigated by subsetting the PBMC dataset to those clusters identified
784 as neutrophils and pre-neutrophils (cluster 9 and 13). Within those subsets, we selected top 2000
785 variable genes and repeated a clustering using the SNN-graph based Louvain algorithm
786 mentioned above with a resolution of 0.6. The dimensionality of the data was then reduced to 10
787 PCs, which served as input for the UMAP calculation. To categorize the observed neutrophil
788 clusters into the respective cell cycle states, we applied the CellCycleScoring function of Seurat
789 and visualized the results as pie charts.

790 A gene signature enrichment analysis using the 'AUCCell' method (Aibar et al., 2017) was applied
791 to link observed neutrophil clusters to existing studies and neutrophils of cohort 2. We set the
792 threshold for the calculation of the area under the curve (AUC) to marker genes from collected
793 publications and top 30 of the ranked marker genes from each of neutrophil clusters from cohort
794 2. The resulting AUC values were normalized the maximum possible AUC to 1 and subsequently
795 visualized in violin plots or UMAP plots.

796

797

798 ***ScRNA-seq data analysis of Rhapsody data of cohort 2***

799 ***General steps for Rhapsody data downstream analysis***

800 ScRNA-seq UMI count matrices were imported to R 3.6.2 and gene expression data analysis was
801 performed using the R/Seurat package 3.1.2 (Butler et al., 2018). Demultiplexing of cells was
802 performed using the *HTODemux* function implemented in Seurat. After identification of singlets,
803 cells with more than 25% mitochondrial reads, less than 250 expressed genes or more than 5000
804 expressed genes were excluded from the analysis and only those genes present in more than 5
805 cells were considered for downstream analysis. The following normalization, scaling and
806 dimensionality reduction steps were performed independently for each of the data subsets used
807 for the different analyses as indicated respectively. In general, gene expression values were
808 normalized by total UMI counts per cell, multiplied by 10,000 (TP10K) and then log transformed
809 by $\log_{10}(TP10k+1)$. Subsequently, the data was scaled, centered and regressed against the
810 number of detected genes per cell to correct for heterogeneity associated with differences in
811 sequencing depth. For dimensionality reduction, PCA was performed on the top 2000 variable
812 genes identified using the *vst* method implemented in Seurat. Subsequently, UMAP was used for
813 two-dimensional representation of the data structure. No batch effect removal or data integration
814 analysis was performed on the BD Rhapsody data. Cell type annotation was based on the
815 respective clustering results combined with data-driven cell type classification algorithms based
816 on reference transcriptomes data (Aran et al., 2019) and expression of known marker genes.

817 ***scRNA-seq analysis of the complete BD rhapsody data set of cohort 2 including data from***
818 ***frozen and fresh PBMC and whole blood***

819 ScRNA-seq count data of 162,797 cells derived from fresh and frozen PBMC samples purified by
820 density gradient centrifugation and whole blood after erythrocyte lysis of cohort 2 (Bonn, BD
821 Rhapsody) were combined, normalized and scaled as described above. After variable gene
822 selection and PCA, UMAP was performed based on the first 25 principal components (PCs). No
823 batch correction or data integration strategies were applied to the data. Separate visualization of
824 the cells showed overlay of cells unaffected by the technical differences in sample handling. Data
825 quality and information content was visualized as violin plots showing the number of detected
826 genes and transcripts (UMIs) per sample handling strategy split by PBMC and granulocyte
827 fraction.

828 ***scRNA-seq analysis of fresh and frozen PBMC samples***

829 ScRNA-seq count data of 93,297 cells derived from fresh and frozen PBMC samples of cohort 2
830 (Bonn, BD Rhapsody) purified by density gradient centrifugation were normalized and scaled as
831 described above. After variable gene selection and PCA, UMAP was performed and the cells
832 were clustered using the Louvain algorithm based on the first 15 PCs and a resolution of 0.5.
833 Cluster identities were determined by reference-based cell classification and inference of cluster-
834 specific marker genes using the Wilcoxon rank sum test using the following cutoffs: genes have
835 to be expressed in more than 20% of the cells of the respective cluster, exceed a logarithmic
836 fold change cutoff to at least 0.25, and exhibited a difference of > 10% in the detection between
837 two clusters.

838 ***Quantification of the percentages of cell clusters in the PBMC scRNA-seq data of both***
839 ***cohorts separated by disease group***

840 To compare shifts in the monocyte and neutrophil populations in the PBMC compartment of
841 COVID-19 patients, the percentages of the cellular subsets - as identified by clustering and cluster
842 annotation explained above for the two independent scRNA-seq data sets (cohort 1 and cohort
843 2) - of the total number of PBMC in each data set were quantified per sample and visualized
844 together in box plots. Statistical significance was inferred using *t*-test.

845 ***Subset analysis of the monocytes within the PBMC data set of cohort 2***

846 The monocyte space was investigated by subsetting the PBMC dataset to those clusters identified
847 as monocytes (cluster 1, 3, 5, 9, and 12) and repeating the variable gene selection (top 2000
848 variable genes), regression for the number of UMIs and scaling as described above. The
849 dimensionality of the data was then reduced to 8 PCs, which served as input for the UMAP
850 calculation. The SNN-graph based Louvain clustering of the monocytes was performed using a
851 resolution of 0.48. Marker genes per cluster were calculated using the Wilcoxon rank sum test
852 using the following cutoffs: genes have to be expressed in > 20% of the cells, exceed a
853 logarithmic fold change cutoff to at least 0.25, and exhibited a difference of > 10% in the detection
854 between two clusters.

855 ***Time kinetics analysis of identified monocyte clusters***

856 For each patient and time point of sample collection, the proportional occupancy of the monocyte
857 clusters was calculated, and the relative proportions were subsequently visualized as a function
858 of time.

859 ***Analysis of the scRNA-seq data from fresh PBMC and whole blood samples of cohort 2***

860 ScRNA-seq count data derived from fresh PBMC samples purified by density gradient
861 centrifugation and whole blood after erythrocyte lysis of cohort 2 (BD Rhapsody) were normalized,
862 scaled, and regressed for the number of UMI per cell as described above. After PCA based on
863 the top 2000 variable genes, UMAP was performed using the first 15 PCs. Cell clusters were
864 determined using Louvain clustering implemented in Seurat based on the first 15 principle
865 components and a resolution of 0.5. Cluster identities were assigned as detailed above using
866 reference-based classification and marker gene expression. Subsequently, the dataset was
867 subsetted for clusters identified as neutrophils and pre-neutrophils, and re-scaled and regressed.
868 After PCA on the top 2000 variable genes, UMAP was performed on the first 15 PCs. Clustering
869 was performed as described above on the top 15 PCs using a resolution of 0.5. Clusters featuring
870 high counts in hemoglobin genes and expression of the eosinophil specific marker gene CLC
871 were excluded from subsequent analyses. After filtering and rescaling of the neutrophil
872 compartment a division of the cells according to experimental batches was observed in the
873 two-dimensional UMAP representation. Comparing experimental procedures of different
874 experiments pointed to short-term storage of whole blood on ice for a single experimental
875 batch as a technical influence potentially explaining the transcriptional differences. Therefore,
876 cells from the respective experiment were excluded, reducing the number of samples to a
877 total of 15 (30,019 cells, 10 controls, 5 COVID-19 patients) to prevent any technical bias from
878 skewing the analysis. After exclusion, the remaining data were processed as described above
879 and clustered using Louvain clustering based on the first 15 PCs with a resolution of 0.7 was
880 performed.

881 Differentially expressed genes between clusters were defined using a Wilcoxon rank sum test for
882 differential gene expression implemented in Seurat. Genes had to be expressed in >10% of the
883 cells of a cluster, exceed a logarithmic threshold >0.1 and to have >10% difference in the minimum
884 detection between two clusters.

885 ***Quantification of the percentages of cell subsets in the fresh whole blood scRNA-seq data***
886 ***of cohort 2***

887 After cell type classification of the combined scRNA-seq data set of fresh PBMC and whole blood
888 samples of cohort 2 described above, 69,500 cells derived from whole blood samples after
889 erythrocyte lysis were subsetted. Percentages of cell subsets in those whole blood samples of
890 the total number of cells were quantified per sample and visualized in box plots separated by
891 disease stage and group.

892 ***Confusion matrix***

893 For each cluster of neutrophils, the relative proportion across disease severity and time point was
894 visualized as a fraction of samples from the respective condition contributing to the cluster.

895 ***GO enrichment***

896 Gene set enrichment was performed on gene sets from the Kyoto Encyclopedia of Genes and
897 Genomes (KEGG) database (Kanehisa, 2019), Hallmark gene sets (Liberzon et al., 2015) and
898 Gene Ontology (GO) (Ashburner et al., 2000; Carbon et al., 2019) using the R
899 package/ClusterProfiler v.3.10.1 (Yu et al., 2012).

900 ***Cell cycle state analysis of scRNA-Seq data***

901 To categorize the cells within the neutrophil clusters into the respective cell cycle states, we
902 applied the *CellCycleScoring* function of Seurat and visualized the results as pie charts.

903 ***Trajectory analysis***

904 Trajectory analysis was performed using the *destiny* algorithm (Angerer et al., 2016). In brief, the
905 neutrophil space was subsetted to only severe patients (early and mild) and only the most
906 prominent clusters of the latter (clusters 9,8,2,0,6). The normalized data were scaled and
907 regressed for UMIs and a diffusion map was calculated based on the top 2,000 variable genes
908 with a sum of at least 10 counts over all cells. Based on the diffusion map, a diffusion pseudo
909 time was calculated (without fixing a starting point) to infer a transition probability between the
910 different cell states of the neutrophils. Subsequently, the density of the clusters along the
911 pseudotime and marker gene expression for each cluster were visualized.

912 Enrichment of gene sets was performed using the 'AUCCell' method (Aibar et al., 2017)
913 implemented in the package (version 1.4.1) in R. We set the threshold for the calculation of the
914 AUC to the top 3% of the ranked genes and normalized the maximum possible AUC to 1. The
915 resulting AUC values were subsequently visualized in violin plots or UMAP plots.

916 ***Transcription factor prediction analysis***

917 The Cytoscape (version v3.7.1, doi: 10.1101/gr.1239303) plug-in iRegulon (Janky et al., 2014)
918 (version 1.3) was used to predict the transcription factors potentially regulating cluster-specifically
919 expressed gene sets in the neutrophil subset analysis in cohort 2. The genomic regions for TF-
920 motif search were limited to 10 kbp around the respective transcriptional start sites and filtered
921 for predicted TFs with a normalized enrichment score > 4.0. Next, we filtered for TFs, which
922 exceeded a cumulative normalized expression cutoff of 50 in the respective neutrophil cluster.
923 Subsequently, we selected transcription factors of known relevance in the context of neutrophil
924 biology and constructed a network linking target genes among the cluster-specifically expressed
925 marker genes and their predicted and expressed regulators for visualization in Cytoscape.

926 ***Mass cytometry data analysis***

927 Cytobank.org was used for de-barcoding of individual samples and manually gating of cell events
928 to remove doublets, normalization beads and dead cells (Kotecha et al., 2010). For semi-
929 automated gating of populations of interest, high-resolution SPADE clustering was conducted on
930 all indicated markers (supplementary table 2) with 400 target nodes. Individual SPADE nodes
931 were then aggregated and annotated to cell subsets (bubbles) according to the expression of
932 lineage-specific differentiation markers.

933 To generate tSNE maps viSNE analysis was performed using the indicated markers
934 (supplementary table 2). Embedding parameters were set to at least 1000 iterations per 100.000
935 analyzed cells, perplexity of 30 and theta of 0.5. For statistical analysis of cell population
936 abundances, we fitted a generalized linear mixed-effects model (GLMM) for each population using
937 the lme4 package as previously described by Nowicka et. al (Robinson et al., 2017).

938 **Data Analysis of Flow Cytometry Data**

939 Flow cytometry data analysis was performed with FlowJo V10.6.1. Relative cell percentage or
940 mean fluorescence intensity (MFI) was used for visualization and statistical analysis. Cell type
941 was defined as granulocytes (CD45⁺, CD66b⁺), non-classical monocytes (CD45⁺, CD66b⁻, CD19⁻
942 , CD3⁻, CD56⁻, CD14^{dim}, CD16⁺).

943 **Data visualization**

944 In general, the R packages Seurat and the ggplot2 package (version 3.1.0, Wickham, 2016) were
945 used to generate figures. For visualization of mass cytometry data, cluster minimum-spanning
946 trees were rendered using Cytobank, the ComplexHeatmap package was used to display subset
947 phenotypes and GraphPad Prism to generate boxplots of quantitative data.

948 **Lead Contact**

949 Further information and requests for resources and reagents should be directed to the Lead
950 Contact, **Joachim L. Schultze**

951 **Data Availability**

952 Data are deposited at the European Genome-phenome Archive (EGA) under access number
953 EGAS00001004450, which is hosted by the EBI and the CRG.

954

955 **KEY RESOURCES TABLE**

REAGENT or RESOURCE	SOURCE	IDENTIFIER
Antibodies		
HLA-DR BV421 (L243)	Biolegend	307635 (AB_10897449)
CD4 BV510 (OKT4)	Biolegend	317444 (AB_2561866)
CD16 BV605 (3G8)	Biolegend	302039 (AB_2561354)
CD45 BV711 (HI30)	Biolegend	304050 (AB_2563466)
CD8 BV785 (SK1)	Biolegend	344740 (AB_2566202)
CD66b FITC (G10F5)	Biolegend	305104 (AB_314496)
CD14 PerCp-Cy5.5 (MφP9)	Becton Dickinson	562692 (AB_2737726)
CD56 PE (MY31)	Becton Dickinson	345810 (AB_396511)
CD3 PE/Dazzle (UCHT1)	Biolegend	300450 (AB_2563618)
CD11c PE/Cy5 (B-ly6)	Becton Dickinson	551077 (AB_394034)
Siglec8 PE/Cy7 (7C9)	Biolegend	347112 (AB_2629720)
CD203c APC (NP4D6)	Biolegend	324609 (AB_2099774)
CD1c AlexaFluor700 (L161)	Biolegend	331530 (AB_2563657)
CD19 APC/Fire 750 (HIB19)	Biolegend	302258 (AB_2629691)
CD45 89Y (HI30)	Fluidigm	3089003B

HLADR purified (L243)	Biolegend	307602
CD3 purified (UCHT1)	Biolegend	300443
CD196 141Pr (G034E3)	Fluidigm	3141003A
CD19 142Nd (HIB-19)	Fluidigm	3142001B
CD123 143Nd (6H6)	Fluidigm	3143014B
CD15 144Nd (W6D3)	Fluidigm	3144019B
CD138 145Nd (DL101)	Fluidigm	3145003B
CD64 146Nd (10.1)	Fluidigm	3146006B
CD21 purified (Bu32)	Biolegend	354902
CD226 purified (REA1040)	Miltenyi Biotec	Produced at request
IgD purified (IgD26)	Biolegend	348235
ICOS 148Nd (C398.4A)	Fluidigm	3148019B
CD206 purified (152)	Biolegend	321127
CD96 purified (REA195)	Miltenyi Biotec	Produced at request
KLRG1 purified (REA261)	Miltenyi Biotec	Produced at request
TCRgd purified (11F2)	Miltenyi Biotec	Produced at request
FcεRI 150Nd (AER-37)	Fluidigm	3150027B
CD155 purified (REA1081)	Miltenyi Biotec	Produced at request
CD95 purified (DX2)	Biolegend	305631

TIGIT 153Eu (MBSA43)	Fluidigm	3153019B
CD62L 153Eu (DREG56)	Fluidigm	3153004B
CD62L purified (DREG56)	Biolegend	304835
CD1c purified (L161)	Biolegend	331502
CD27 155Gd (L128)	Fluidigm	3155001B
CXCR3 156Gd (G025H7)	Fluidigm	3156004B
KLRF1 purified (REA845)	Miltenyi Biotec	Produced at request
CD10 158Gd (HI10a)	Fluidigm	3158011B
CD33 158Gd (WM53)	Fluidigm	3158001B
CD14 160Gd (RMO52)	Fluidigm	3160006B
CD28 purified (L293)	BD Bioscience	348040
CD69 162Dy (FN50)	Fluidigm	3162001B
CD294 163Dy (BM16)	Fluidigm	3163003B
RANKL APC	Miltenyi Biotec	130-098-511
Anti-APC 163Dy	Fluidigm	3163001B
CXCR5 164Dy (51505)	Fluidigm	3164029B
Siglec 8 164Dy (7C9)	Fluidigm	3164017B
CD34 166Er (581)	Fluidigm	3166012B
CD38 167Er (HIT2)	Fluidigm	3167001B

Ki67 168Er (Ki-67)	Fluidigm	3168007B
CD25 169Tm (2A3)	Fluidigm	3169003B
CD24 169Tm (ML5)	Fluidigm	3169004B
Lag3 purified (11C3C65)	Biolegend	369302
RANK purified (80704)	R&D Systems	MAB683
CD161 purified (HP-3G10)	Biolegend	339919
CD11b purified (ICRF44)	Biolegend	301337
CD45RO purified (4G11)	DRFZ Berlin	
CD44 purified (BJ18)	Biolegend	338811
CD137 173Yb (4B4-1)	Fluidigm	3173015B
PD-1 175Lu (EH12.2H7)	Fluidigm	3175008B
PD-L1 175Lu (29.E2A3)	Fluidigm	3175017B
CD56 176Yb (NCAM16.2)	Fluidigm	3176008B
CD8A purified (GN11)	DRFZ Berlin	
IgM purified (MHM-88)	Biolegend	314502
CD11c purified (Bu15)	Biolegend	337221
B2M purified (2M2)	Biolegend	316302
CD16 209Bi (3G8)	Fluidigm	3209002B
A0251 anti-human Hashtag 1	Biolegend	394601

A0252 anti-human Hashtag 2	Biolegend	394603
A0253 anti-human Hashtag 3	Biolegend	394605
A0254 anti-human Hashtag 4	Biolegend	394607
A0255 anti-human Hashtag 5	Biolegend	394609
A0256 anti-human Hashtag 6	Biolegend	394611
A0257 anti-human Hashtag 7	Biolegend	394613
CD235ab Biotin (HIR2)	Biolegend	306618
Bacterial and Virus Strains		
Biological Samples		
Chemicals, Peptides, and Recombinant Proteins		
BD Horizon Brilliant™ Stain Buffer	Becton Dickinson	563794
RBC lysis buffer 10X	Biolegend	420301
Pierce™ 16% Formaldehyde (w/v), Methanol-free	Thermo Fisher	28908
RPMI 1640 Medium	Gibco	11875093
Fetal Bovine Serum	PAN Biotec	3302

Stain Buffer (FBS)	Becton Dickinson	554656
Pancoll human, Density: 1.077 g/ml	Pan Biotech	P04-601000
Dulbecco'S Phosphate Buffered Saline, MO	Sigma-Aldrich	D8537
FcR Blocking Reagent, human	Miltenyi	130-059-901
Live/Dead mDOTA 103Rh	In-house	
Cell-ID Intercalator-Ir	Fluidigm	201192A
Permeabilization buffer 10X	eBioscience	00-8333-56
Maxpar PBS	Fluidigm	201058
Maxpar Cell Staining buffer	Fluidigm	201068
Maxpar X8 Multimetal Labeling Kit	Fluidigm	201300
Proteomic stabilizer	Smart Tube Inc.	PROT1
Nuclease-Free Water	Invitrogen	AM9937
KAPA HiFi HotStart Ready Mix	Roche	KK2601
Human Tru Stain FcX	Biologend	422301
TE Buffer	Thermo Fisher	120900115
SPRIselect Reagent	Invitrogen	AM9937
10% Tween 20	BIO-RAD	1662404
Buffer EB	Qiagen	19086
Ethanol, Absolute	Fisher Bioreagents	BP2818-500

Glycerol, 85%	Merck	1040941000
Bovine Serum Albumin	Jackson Immuno Research	001-000-161
Tween20	Sigma-Aldrich	P1379-500M
MagniSort™ Negative Selection Beads	Thermo Fisher	MSNB-6002-74
Critical Commercial Assays		
LIVE/DEAD Fixable Yellow Dead Cell Stain Kit	Thermo Fisher	L34967
Human Single-Cell Multiplexing Kit	BD	633781
BD Rhapsody™ WTA Amplification Kit	BD	633801
BD Rhapsody Cartridge Kit	BD	633733
BD Rhapsody cDNA Kit	BD	633773
High Sensitivity D5000 ScreenTape	Agilent	5067-5592
Qubit dsDNA HS Assay Kit	ThermoFisher	Q32854
Chromium Next GEM Single Cell 3' GEM, Library & Gel Bead Kit v3.1	10x genomics	1000121
Chromium Next GEM Chip G Single Cell Kit	10x genomics	1000120
Single Index Kit T Set A	10x genomics	1000213
High Sensitivity DNA Kit	Agilent	5067-4626
NovaSeq 6000 S1 Reagent Kit (100 cycle)	Illumina	200012865
NovaSeq 6000 S2 Reagent Kit (100 cycle)	Illumina	20012862

NovaSeq 6000 S2 Reagent Kit (200 cycles)	Illumina	20040326
NovaSeq 6000 S2 Reagent Kit (200 cycles)	Illumina	20040326
NextSeq 500/550 High Output Kit v2.5 (150 Cycles)	Illumina	20024907
Deposited Data		
RNA-Seq raw data	This paper	EGAS00001004450
Experimental Models: Cell Lines		
Experimental Models: Organisms/Strains		
Oligonucleotides		
SI-PCR primer	IDT	AATGATACGGCG ACCACCGAGATC TACTACTACTCT TTCCCTACACGAC GC*T*C
HTO additive primer	IDT	GTGACTGGAGTT CAGACGTGTGC*T *C
D701_S	IDT	CAAGCAGAAGAC GGCATACGAGAT CGAGTAATGTGA CTGGAGTTCAGA CGTGT*G*C

D702_S	IDT	CAAGCAGAAGAC GGCATACGAGAT TCTCCGGAGTGA CTGGAGTTCAGA CGTGT*G*C
D703_S	IDT	CAAGCAGAAGAC GGCATACGAGAT AATGAGCGGTGA CTGGAGTTCAGA CGTGT*G*C
D705_S	IDT	CAAGCAGAAGAC GGCATACGAGAT TTCTGAATGTGAC TGGAGTTCAGAC GTGT*G*C
Recombinant DNA		
Software and Algorithms		
Seurat (R package)	CRAN	v3.1.4
Seurat (R package)	CRAN	v3.1.2
ClusterProfiler (R package)	CRAN	v3.10.1
DirichletReg (R package)	CRAN	v0.6.3.1
AUCCell (R package)	CRAN	v1.6.1
Cytobank (software)	Kotecha N, et al., Curr Protoc Cytom. 2010	https://doi.org/10.1002/0471142956.cy1017s53

	https://www.cytobank.org	
SPADE (Cytobank)	Qiu P, et al., Nat Biotechnol. 2011	https://doi.org/10.1038/nbt.1991
viSNE (Cytobank)	Amir el-AD, et al., Nat Biotechnol. 2013	https://doi.org/10.1038/nbt.2594
flowCore (R package)	Bioconductor	v1.48.1
CytoML (R package)	Bioconductor	v1.8.1
flowFP (R package)	Bioconductor	v1.40.1
ComplexHeatmap (R package)	Bioconductor	v1.20.0
lme4 (R package)	CRAN	v1.1-21
Prism (software)	www.graphpad.com	v8
Other		

956

957 **References**

- 958 Ahmad, S., Singh, P., Sharma, A., Arora, S., Shriwash, N., Rahmani, A.H., Almatroodi, S.A.,
959 Manda, K., Dohare, R., and Syed, M.A. (2019). Transcriptome meta-analysis deciphers a
960 dysregulation in immune response-associated gene signatures during sepsis. *Genes (Basel)*.
961 *10*, 1005.
- 962 Aibar, S., González-Blas, C.B., Moerman, T., Huynh-Thu, V.A., Imrichova, H., Hulselmans, G.,
963 Rambow, F., Marine, J.C., Geurts, P., Aerts, J., et al. (2017). SCENIC: Single-cell regulatory
964 network inference and clustering. *Nat. Methods* *14*, 1083–1086.
- 965 Alder, M.N., Opoka, A.M., Lahni, P., Hildeman, D.A., and Wong, H.R. (2017). Olfactomedin-4 Is
966 a Candidate Marker for a Pathogenic Neutrophil Subset in Septic Shock. *Crit. Care Med.* *45*,
967 e426–e432.
- 968 Allan, R.P., Barlow, M., Byrne, M.P., Cherchi, A., Douville, H., Fowler, H.J., Gan, T.Y.,
969 Pendergrass, A.G., Rosenfeld, D., Swann, A.L.S., et al. (2020). Advances in understanding
970 large-scale responses of the water cycle to climate change. *Ann. N. Y. Acad. Sci.*
- 971 Angerer, P., Haghverdi, L., Büttner, M., Theis, F.J., Marr, C., and Büttner, F. (2016). Destiny:
972 Diffusion maps for large-scale single-cell data in R. *Bioinformatics* *32*, 1241–1243.
- 973 Aran, D., Looney, A.P., Liu, L., Wu, E., Fong, V., Hsu, A., Chak, S., Naikawadi, R.P., Wolters,
974 P.J., Abate, A.R., et al. (2019). Reference-based analysis of lung single-cell sequencing reveals
975 a transitional profibrotic macrophage. *Nat. Immunol.* *20*, 163–172.
- 976 Ashburner, M., Ball, C.A., Blake, J.A., Botstein, D., Butler, H., Cherry, J.M., Davis, A.P., Dolinski,
977 K., Dwight, S.S., Eppig, J.T., et al. (2000). Gene ontology: Tool for the unification of biology. *Nat.*
978 *Genet.* *25*, 25–29.
- 979 Barnes, B.J., Adrover, J.M., Baxter-Stoltzfus, A., Borczuk, A., Cools-Lartigue, J., Crawford, J.M.,
980 Daßler-Plenker, J., Guerci, P., Huynh, C., Knight, J.S., et al. (2020). Targeting potential drivers
981 of COVID-19: Neutrophil extracellular traps. *J. Exp. Med.* *217*.
- 982 Bowers, N.L., Helton, E.S., Huijbregts, R.P.H., Goepfert, P.A., Heath, S.L., and Hel, Z. (2014).
983 Immune Suppression by Neutrophils in HIV-1 Infection: Role of PD-L1/PD-1 Pathway. *PLoS*
984 *Pathog.* *10*.
- 985 Braun, J., Loyal, L., Frentsch, M., Wendisch, D., Georg, P., Kurth, F., Hippenstiel, S., Dingeldey,
986 M., Kruse, B., Fauchere, F., et al. (2020). Presence of SARS-CoV-2 reactive T cells in COVID-
987 19 patients and healthy donors. *MedRxiv* 2020.04.17.20061440.
- 988 Brignola, C., Campieri, M., Farruggia, P., Tragnone, A., Pasquali, S., Iannone, P., Lanfranchi,
989 G.A., and Barbara, L. (1988). The possible utility of steroids in the prevention of relapses of
990 crohn's disease in remission: A preliminary study. *J. Clin. Gastroenterol.* *10*, 631–634.
- 991 Bronte, V., Serafini, P., Mazzoni, A., Segal, D.M., and Zanovello, P. (2003). L-arginine metabolism
992 in myeloid cells controls T-lymphocyte functions. *Trends Immunol.* *24*, 301–305.
- 993 Butler, A., Hoffman, P., Smibert, P., Papalexi, E., and Satija, R. (2018). Integrating single-cell
994 transcriptomic data across different conditions, technologies, and species. *Nat. Biotechnol.* *36*,
995 411–420.
- 996 Carbon, S., Douglass, E., Dunn, N., Good, B., Harris, N.L., Lewis, S.E., Mungall, C.J., Basu, S.,
997 Chisholm, R.L., Dodson, R.J., et al. (2019). The Gene Ontology Resource: 20 years and still
998 GOing strong. *Nucleic Acids Res.* *47*, D330–D338.
- 999 Cassetta, L., Baekkevold, E.S., Brandau, S., Bujko, A., Cassatella, M.A., Dorhoi, A., Krieg, C.,
1000 Lin, A., Loré, K., Marini, O., et al. (2019). Deciphering myeloid-derived suppressor cells: isolation
1001 and markers in humans, mice and non-human primates. *Cancer Immunol. Immunother.* *68*,
1002 687–697.

- 1003 Chen, G., Wu, D., Guo, W., Cao, Y., Huang, D., Wang, H., Wang, T., Zhang, X., Chen, H., Yu,
1004 H., et al. (2020). Clinical and immunologic features in severe and moderate Coronavirus Disease
1005 2019. *J. Clin. Invest.*
- 1006 Darcy, C.J., Minigo, G., Piera, K.A., Davis, J.S., McNeil, Y.R., Chen, Y., Volkheimer, A.D.,
1007 Weinberg, J.B., Anstey, N.M., and Woodberry, T. (2014). Neutrophils with myeloid derived
1008 suppressor function deplete arginine and constrain T cell function in septic shock patients. *Crit.*
1009 *Care* 18, R163.
- 1010 Dimopoulos, G., de Mast, Q., Markou, N., Theodorakopoulou, M., Komnos, A., Mouktaroudi, M.,
1011 Netea, M.G., Spyridopoulos, T., Verheggen, R.J., Hoogerwerf, J., et al. (2020). FAVORABLE
1012 ANAKINRA RESPONSES IN SEVERE COVID-19 PATIENTS WITH SECONDARY
1013 HEMOPHAGOCYTIC LYMPHOHISTIOCYTOSIS. *Cell Host Microbe*.
- 1014 Fauver, J.R., Petrone, M.E., Hodcroft, E.B., Shioda, K., Ehrlich, H.Y., Watts, A.G., Vogels, C.B.F.,
1015 Brito, A.F., Alpert, T., Muyombwe, A., et al. (2020). Coast-to-Coast Spread of SARS-CoV-2
1016 during the Early Epidemic in the United States. *Cell*.
- 1017 Giamarellos-Bourboulis, E.J., Netea, M.G., Rovina, N., Akinosoglou, K., Antoniadou, A.,
1018 Antonakos, N., Damoraki, G., Gkavogianni, T., Adami, M.E., Katsaounou, P., et al. (2020).
1019 Complex Immune Dysregulation in COVID-19 Patients with Severe Respiratory Failure. *Cell*
1020 *Host Microbe*.
- 1021 Grifoni, A., Weiskopf, D., Ramirez, S.I., Mateus, J., Dan, J.M., Moderbacher, C.R., Rawlings, S.A.,
1022 Sutherland, A., Premkumar, L., Jadi, R.S., et al. (2020). Targets of T cell responses to SARS-
1023 CoV-2 coronavirus in humans with COVID-19 disease and unexposed individuals. *Cell*.
- 1024 Guan, W.J., Ni, Z.Y., Hu, Y., Liang, W.H., Ou, C.Q., He, J.X., Liu, L., Shan, H., Lei, C.L., Hui,
1025 D.S.C., et al. (2020a). Clinical Characteristics of Coronavirus Disease 2019 in China. *N. Engl.*
1026 *J. Med.*
- 1027 Guan, W.J., Liang, W.H., Zhao, Y., Liang, H.R., Chen, Z.S., Li, Y.M., Liu, X.Q., Chen, R.C., Tang,
1028 C.L., Wang, T., et al. (2020b). Comorbidity and its impact on 1590 patients with Covid-19 in
1029 China: A Nationwide Analysis. *Eur. Respir. J.*
- 1030 Hadjadj, J., Yatim, N., Barnabei, L., Corneau, A., Boussier, J., Pere, H., Charbit, B., Bondet, V.,
1031 Chenevier-Gobeaux, C., Breillat, P., et al. (2020). Impaired type I interferon activity and
1032 exacerbated inflammatory responses in severe Covid-19 patients. *MedRxiv*
1033 2020.04.19.20068015.
- 1034 Hafemeister, C., and Satija, R. (2019). Normalization and variance stabilization of single-cell
1035 RNA-seq data using regularized negative binomial regression. *Genome Biol.* 20.
- 1036 Hartung, T., Döcke, W.D., Gantner, F., Krieger, G., Sauer, A., Stevens, P., Volk, H.D., and
1037 Wendel, A. (1995). Effect of granulocyte colony-stimulating factor treatment on ex vivo blood
1038 cytokine response in human volunteers. *Blood* 85, 2482–2489.
- 1039 Hesselink, L., Spijkerman, R., Van Wessel, K.J.P., Koenderman, L., Leenen, L.P.H., Huber-
1040 Lang, M., and Hietbrink, F. (2019). Neutrophil heterogeneity and its role in infectious
1041 complications after severe trauma. *World J. Emerg. Surg.* 14.
- 1042 Hoffmann, M., Kleine-Weber, H., Schroeder, S., Krüger, N., Herrler, T., Erichsen, S., Schiergens,
1043 T.S., Herrler, G., Wu, N.H., Nitsche, A., et al. (2020). SARS-CoV-2 Cell Entry Depends on ACE2
1044 and TMPRSS2 and Is Blocked by a Clinically Proven Protease Inhibitor. *Cell* 181, 271-280.e8.
- 1045 Hoffmann, S., Harms, H., Ulm, L., Nabavi, D.G., Mackert, B.M., Schmehl, I., Jungehulsing, G.J.,
1046 Montaner, J., Bustamante, A., Hermans, M., et al. (2017). Stroke-induced immunodepression
1047 and dysphagia independently predict stroke-associated pneumonia – The PREDICT study. *J.*
1048 *Cereb. Blood Flow Metab.* 37, 3671–3682.
- 1049 Huang, C., Wang, Y., Li, X., Ren, L., Zhao, J., Hu, Y., Zhang, L., Fan, G., Xu, J., Gu, X., et al.

- 1050 (2020). Clinical features of patients infected with 2019 novel coronavirus in Wuhan, China.
1051 *Lancet* 395, 497–506.
- 1052 Jamilloux, Y., Henry, T., Belot, A., Viel, S., Fauter, M., El Jammal, T., Walzer, T., François, B.,
1053 and Sève, P. (2020). Should we stimulate or suppress immune responses in COVID-19?
1054 Cytokine and anti-cytokine interventions. *Autoimmun. Rev.* 102567.
- 1055 Kamp, V.M., Pillay, J., Lammers, J.-W.J., Pickkers, P., Ulfman, L.H., and Koenderman, L. (2012).
1056 Human suppressive neutrophils CD16 bright /CD62L dim exhibit decreased adhesion . *J.*
1057 *Leukoc. Biol.* 92, 1011–1020.
- 1058 Kanehisa, M. (2019). Toward understanding the origin and evolution of cellular organisms. *Protein*
1059 *Sci.* 28, 1947–1951.
- 1060 Kangelaris, K.N., Prakash, A., Liu, K.D., Aouizerat, B., Woodruff, P.G., Erle, D.J., Rogers, A.,
1061 Seeley, E.J., Chu, J., Liu, T., et al. (2015). Increased expression of neutrophil-related genes in
1062 patients with early sepsis-induced ARDS. *Am. J. Physiol. - Lung Cell. Mol. Physiol.* 308, L1102–
1063 L1113.
- 1064 Klok, F.A., Kruij, M.J.H.A., van der Meer, N.J.M., Arbous, M.S., Gommers, D.A.M.P.J., Kant,
1065 K.M., Kaptein, F.H.J., van Paassen, J., Stals, M.A.M., Huisman, M. V., et al. (2020). Incidence
1066 of thrombotic complications in critically ill ICU patients with COVID-19. *Thromb. Res.*
- 1067 Kotecha, N., Krutzik, P.O., and Irish, J.M. (2010). Web-based analysis and publication of flow
1068 cytometry experiments. *Curr. Protoc. Cytom.*
- 1069 Kurth, F., Roennefarth, M., Thibeault, C., Corman, V.M., Mueller-Redetzky, H., Mittermaier, M.,
1070 Ruwwe-Gloesenkamp, C., Krannich, A., Schmidt, S., Kretzler, L., et al. (2020). Studying the
1071 pathophysiology of coronavirus disease 2019 - a protocol for the Berlin prospective COVID-19
1072 patient cohort (Pa- COVID-19). *MedRxiv* 2020.05.06.20092833.
- 1073 Kverneland, A.H., Streit, M., Geissler, E., Hutchinson, J., Vogt, K., Boës, D., Niemann, N.,
1074 Pedersen, A.E., Schlickeiser, S., and Sawitzki, B. (2016). Age and gender leucocytes variances
1075 and references values generated using the standardized ONE-Study protocol. *Cytom. Part A*
1076 89, 543–564.
- 1077 Leshner, M., Wang, S., Lewis, C., Zheng, H., Chen, X.A., Santy, L., and Wang, Y. (2012). PAD4
1078 mediated histone hypercitullination induces heterochromatin decondensation and chromatin
1079 unfolding to form neutrophil extracellular trap-like structures. *Front. Immunol.* 3.
- 1080 Li, W., Moore, M.J., Vaslieva, N., Sui, J., Wong, S.K., Berne, M.A., Somasundaran, M., Sullivan,
1081 J.L., Luzuriaga, K., Greeneugh, T.C., et al. (2003). Angiotensin-converting enzyme 2 is a
1082 functional receptor for the SARS coronavirus. *Nature* 426, 450–454.
- 1083 Li, X.K., Lu, Q. Bin, Chen, W.W., Xu, W., Liu, R., Zhang, S.F., Du, J., Li, H., Yao, K., Zhai, D., et
1084 al. (2018). Arginine deficiency is involved in thrombocytopenia and immunosuppression in
1085 severe fever with thrombocytopenia syndrome. *Sci. Transl. Med.* 10.
- 1086 Liao, M., Liu, Y., Yuan, J., Wen, Y., Xu, G., Zhao, J., Chen, L., Li, J., Wang, X., Wang, F., et al.
1087 (2020). The landscape of lung bronchoalveolar immune cells in COVID-19 revealed by single-
1088 cell RNA sequencing. *MedRxiv* 2020.02.23.20026690.
- 1089 Liberzon, A., Birger, C., Thorvaldsdóttir, H., Ghandi, M., Mesirov, J.P., and Tamayo, P. (2015).
1090 The Molecular Signatures Database Hallmark Gene Set Collection. *Cell Syst.* 1, 417–425.
- 1091 Loftus, T.J., Mohr, A.M., and Moldawer, L.L. (2018). Dysregulated myelopoiesis and
1092 hematopoietic function following acute physiologic insult. *Curr. Opin. Hematol.* 25, 37–43.
- 1093 Long, Q.-X., Liu, B.-Z., Deng, H.-J., Wu, G.-C., Deng, K., Chen, Y.-K., Liao, P., Qiu, J.-F., Lin, Y.,
1094 Cai, X.-F., et al. (2020). Antibody responses to SARS-CoV-2 in patients with COVID-19. *Nat.*
1095 *Med.* 1–4.
- 1096 Lüdtke, A., Ruibal, P., Becker-Ziaja, B., Rottstegge, M., Wozniak, D.M., Cabeza-Cabrerizo, M.,

- 1097 Thorenz, A., Weller, R., Kerber, R., Idoyaga, J., et al. (2016). Ebola Virus Disease Is
1098 Characterized by Poor Activation and Reduced Levels of Circulating CD16+ Monocytes. *J.*
1099 *Infect. Dis.* *214*, S275–S280.
- 1100 Massoni-Badosa, R., Iacono, G., Moutinho, C., Kulis, M., Palau, N., Marchese, D., Rodríguez-
1101 Ubreva, J., Ballestar, E., Rodríguez-Esteban, G., Marsal, S., et al. (2020). Sampling time-
1102 dependent artifacts in single-cell genomics studies. *Genome Biol.* *21*, 112.
- 1103 McKechnie, J.L., and Blish, C.A. (2020). The innate immune system: fighting on the front lines or
1104 fanning the flames of COVID-19? *Cell Host Microbe*.
- 1105 Mei, H.E., Leipold, M.D., Schulz, A.R., Chester, C., and Maecker, H.T. (2015). Barcoding of Live
1106 Human Peripheral Blood Mononuclear Cells for Multiplexed Mass Cytometry. *J. Immunol.* *194*,
1107 2022–2031.
- 1108 Mei, H.E., Leipold, M.D., and Maecker, H.T. (2016). Platinum-conjugated antibodies for
1109 application in mass cytometry. *Cytom. Part A* *89*, 292–300.
- 1110 Mengos, A.E., Gastineau, D.A., and Gustafson, M.P. (2019). The CD14+HLA-DrIO/NEG
1111 monocyte: An immunosuppressive phenotype that restrains responses to cancer
1112 immunotherapy. *Front. Immunol.* *10*.
- 1113 Merad, M., and Martin, J.C. (2020). Pathological inflammation in patients with COVID-19: a key
1114 role for monocytes and macrophages. *Nat. Rev. Immunol.*
- 1115 Monneret, G., Lepape, A., Voirin, N., Bohé, J., Venet, F., Debard, A.L., Thizy, H., Bienvenu, J.,
1116 Gueyffier, F., and Vanhems, P. (2006). Persisting low monocyte human leukocyte antigen-DR
1117 expression predicts mortality in septic shock. *Intensive Care Med.* *32*, 1175–1183.
- 1118 Naranjo-Gómez, J.S., Castillo, J.A., Rojas, M., Restrepo, B.N., Diaz, F.J., Velilla, P.A., and
1119 Castaño, D. (2019). Different phenotypes of non-classical monocytes associated with systemic
1120 inflammation, endothelial alteration and hepatic compromise in patients with dengue.
1121 *Immunology* *156*, 147–163.
- 1122 Ng, L.G., Ostuni, R., and Hidalgo, A. (2019). Heterogeneity of neutrophils. *Nat. Rev. Immunol.*
1123 *19*, 255–265.
- 1124 Ni, L., Ye, F., Cheng, M.L., Feng, Y., Deng, Y.Q., Zhao, H., Wei, P., Ge, J., Gou, M., Li, X., et al.
1125 (2020). Detection of SARS-CoV-2-Specific Humoral and Cellular Immunity in COVID-19
1126 Convalescent Individuals. *Immunity*.
- 1127 Niu, J., Sun, Y., Chen, B., Zheng, B., Jarugumilli, G.K., Walker, S.R., Hata, A.N., Mino-Kenudson,
1128 M., Frank, D.A., and Wu, X. (2019). Fatty acids and cancer-amplified ZDHHC19 promote STAT3
1129 activation through S-palmitoylation. *Nature*.
- 1130 Pellin, D., Loperfido, M., Baricordi, C., Wolock, S.L., Montepeloso, A., Weinberg, O.K., Biffi, A.,
1131 Klein, A.M., and Biasco, L. (2019). A comprehensive single cell transcriptional landscape of
1132 human hematopoietic progenitors. *Nat. Commun.* *10*.
- 1133 Perlman, S., and Dandekar, A.A. (2005). Immunopathogenesis of coronavirus infections:
1134 Implications for SARS. *Nat. Rev. Immunol.* *5*, 917–927.
- 1135 Pfeiler, S., Massberg, S., and Engelmann, B. (2014). Biological basis and pathological relevance
1136 of microvascular thrombosis. *Thromb. Res.* *133*.
- 1137 Pillay, J., Kamp, V.M., Van Hoffen, E., Visser, T., Tak, T., Lammers, J.W., Ulfman, L.H., Leenen,
1138 L.P., Pickkers, P., and Koenderman, L. (2012). A subset of neutrophils in human systemic
1139 inflammation inhibits T cell responses through Mac-1. *J. Clin. Invest.* *122*, 327–336.
- 1140 Popescu, D.M., Botting, R.A., Stephenson, E., Green, K., Webb, S., Jardine, L., Calderbank, E.F.,
1141 Polanski, K., Goh, I., Efremova, M., et al. (2019). Decoding human fetal liver haematopoiesis.
1142 *Nature* *574*, 365–371.
- 1143 Qi, F., Qian, S., Zhang, S., and Zhang, Z. (2020). Single cell RNA sequencing of 13 human tissues

- 1144 identify cell types and receptors of human coronaviruses. *Biochem. Biophys. Res. Commun.*
- 1145 Remy, K.E., Brakenridge, S.C., Francois, B., Daix, T., Deutschman, C.S., Monneret, G., Jeannet,
1146 R., Laterre, P.-F., Hotchkiss, R.S., and Moldawer, L.L. (2020). Immunotherapies for COVID-19:
1147 lessons learned from sepsis. *Lancet Respir. Med.* 2, 2–5.
- 1148 Reyes, M., Filbin, M.R., Bhattacharyya, R.P., Billman, K., Eisenhaure, T., Hung, D.T., Levy, B.D.,
1149 Baron, R.M., Blainey, P.C., Goldberg, M.B., et al. (2020). An immune-cell signature of bacterial
1150 sepsis. *Nat. Med.* 26, 333–340.
- 1151 Reymond, N., Imbert, A.M., Devilard, E., Fabre, S., Chabannon, C., Xerri, L., Farnarier, C.,
1152 Cantoni, C., Bottino, C., Moretta, A., et al. (2004). DNAM-1 and PVR regulate monocyte
1153 migration through endothelial junctions. *J. Exp. Med.* 199, 1331–1341.
- 1154 Riegel, A., Maurer, T., Prior, B., Stegmaier, S., Heppert, V., Wagner, C., and Hänsch, G.M. (2012).
1155 Human polymorphonuclear neutrophils express RANK and are activated by its ligand, RANKL.
1156 *Eur. J. Immunol.* 42, 975–981.
- 1157 Ritchie, A.I., and Singanayagam, A. (2020). Immunosuppression for hyperinflammation in
1158 COVID-19: a double-edged sword? *Lancet* 395, 1111.
- 1159 Robinson, M.D., Nowicka, M., Krieg, C., Weber, L.M., Hartmann, F.J., Guglietta, S., Becher, B.,
1160 and Levesque, M.P. (2017). CyTOF workflow: Differential discovery in high-throughput high-
1161 dimensional cytometry datasets. *F1000Research* 6.
- 1162 Salomé, B., and Mahmood, Z. (2020). Modulation of immune crosstalk in COVID-19. *Nat. Rev.*
1163 *Immunol.*
- 1164 Sander, L.E., Sackett, S.D., Dierssen, U., Beraza, N., Linke, R.P., Müller, M., Blander, J.M.,
1165 Tacke, F., and Trautwein, C. (2010). Hepatic acute-phase proteins control innate immune
1166 responses during infection by promoting myeloid-derived suppressor cell function. *J. Exp. Med.*
1167 207, 1453–1464.
- 1168 De Santo, C., Salio, M., Masri, S.H., Lee, L.Y.H., Dong, T., Speak, A.O., Porubsky, S., Booth, S.,
1169 Veerapen, N., Besra, G.S., et al. (2008). Invariant NKT cells reduce the immunosuppressive
1170 activity of influenza A virus-induced myeloid-derived suppressor cells in mice and humans. *J.*
1171 *Clin. Invest.* 118, 4036–4048.
- 1172 Scapini, P., Marini, O., Tecchio, C., and Cassatella, M.A. (2016). Human neutrophils in the saga
1173 of cellular heterogeneity: insights and open questions. *Immunol. Rev.* 273, 48–60.
- 1174 Schultze, J.L., Mass, E., and Schlitzer, A. (2019). Emerging Principles in Myelopoiesis at
1175 Homeostasis and during Infection and Inflammation. *Immunity* 50, 288–301.
- 1176 Schulz, A.R., and Mei, H.E. (2019). Surface barcoding of live PBMC for multiplexed mass
1177 cytometry. In *Methods in Molecular Biology*, (Humana Press Inc.), pp. 93–108.
- 1178 Schulz, A.R., Baumgart, S., Schulze, J., Urbicht, M., Grützkau, A., and Mei, H.E. (2019).
1179 Stabilizing Antibody Cocktails for Mass Cytometry. *Cytom. Part A* 95, 910–916.
- 1180 Silvestre-Roig, C., Fridlender, Z.G., Glogauer, M., and Scapini, P. (2019). Neutrophil Diversity in
1181 Health and Disease. *Trends Immunol.* 40, 565–583.
- 1182 Stiel, L., Meziani, F., and Helms, J. (2018). Neutrophil Activation during Septic Shock. *Shock* 49,
1183 371–384.
- 1184 Sungnak, W., Huang, N., Bécavin, C., Berg, M., Queen, R., Litvinukova, M., Talavera-López, C.,
1185 Maatz, H., Reichart, D., Sampaziotis, F., et al. (2020). SARS-CoV-2 entry factors are highly
1186 expressed in nasal epithelial cells together with innate immune genes. *Nat. Med.*
- 1187 Tak, T., Wijten, P., Heeres, M., Pickkers, P., Scholten, A., Heck, A.J.R., Vriskoop, N., Leenen,
1188 L.P., Borghans, J.A.M., Tesselaar, K., et al. (2017). Human CD62Ldim neutrophils identified as
1189 a separate subset by proteome profiling and in vivo pulse-chase labeling. *Blood* 129, 3476–
1190 3485.

- 1191 Testa, U., Riccioni, R., Diverio, D., Rossini, A., Lo Coco, F., and Peschle, C. (2004). Interleukin-
1192 3 receptor in acute leukemia. *Leukemia* 18, 219–226.
- 1193 Thomas, M.P., Whangbo, J., McCrossan, G., Deutsch, A.J., Martinod, K., Walch, M., and
1194 Lieberman, J. (2014). Leukocyte Protease Binding to Nucleic Acids Promotes Nuclear
1195 Localization and Cleavage of Nucleic Acid Binding Proteins. *J. Immunol.* 192, 5390–5397.
- 1196 Uhel, F., Azzaoui, I., Grégoire, M., Pangault, C., Dulong, J., Tadié, J.M., Gacouin, A., Camus, C.,
1197 Cynober, L., Fest, T., et al. (2017). Early expansion of circulating granulocytic myeloid-derived
1198 suppressor cells predicts development of nosocomial infections in patients with sepsis. *Am. J.*
1199 *Respir. Crit. Care Med.* 196, 315–327.
- 1200 Veglia, F., Perego, M., and Gabrilovich, D. (2018). Myeloid-derived suppressor cells coming of
1201 age review-article. *Nat. Immunol.* 19, 108–119.
- 1202 Volkmann, J., Schmitz, J., Nordlohne, J., Dong, L., Helmke, A., Sen, P., Immenschuh, S.,
1203 Bernhardt, W.M., Gwinner, W., Bräsen, J.H., et al. (2020). Kidney injury enhances renal G-CSF
1204 expression and modulates granulopoiesis and human neutrophil CD177 in vivo. *Clin. Exp.*
1205 *Immunol.* 199, 97–108.
- 1206 Wang, B., Li, R., Lu, Z., and Huang, Y. (2020a). Does comorbidity increase the risk of patients
1207 with covid-19: Evidence from meta-analysis. *Aging (Albany, NY).* 12, 6049–6057.
- 1208 Wang, D., Hu, B., Hu, C., Zhu, F., Liu, X., Zhang, J., Wang, B., Xiang, H., Cheng, Z., Xiong, Y.,
1209 et al. (2020b). Clinical Characteristics of 138 Hospitalized Patients with 2019 Novel Coronavirus-
1210 Infected Pneumonia in Wuhan, China. *JAMA - J. Am. Med. Assoc.* 323, 1061–1069.
- 1211 Wilk, A.J., Rustagi, A., Zhao, N.Q., Roque, J., Martinez-Colon, G.J., McKechnie, J.L., Ivison, G.T.,
1212 Ranganath, T., Vergara, R., Hollis, T., et al. (2020). A single-cell atlas of the peripheral immune
1213 response to severe COVID-19. *MedRxiv* 2020.04.17.20069930.
- 1214 Wölfel, R., Corman, V.M., Guggemos, W., Seilmaier, M., Zange, S., Müller, M.A., Niemeyer, D.,
1215 Jones, T.C., Vollmar, P., Rothe, C., et al. (2020). Virological assessment of hospitalized patients
1216 with COVID-2019. *Nature*.
- 1217 Wu, Z., and McGoogan, J.M. (2020). Characteristics of and Important Lessons from the
1218 Coronavirus Disease 2019 (COVID-19) Outbreak in China: Summary of a Report of 72314
1219 Cases from the Chinese Center for Disease Control and Prevention. *JAMA - J. Am. Med. Assoc.*
1220 323, 1239–1242.
- 1221 Wu, F., Zhao, S., Yu, B., Chen, Y.M., Wang, W., Song, Z.G., Hu, Y., Tao, Z.W., Tian, J.H., Pei,
1222 Y.Y., et al. (2020). A new coronavirus associated with human respiratory disease in China.
1223 *Nature* 579, 265–269.
- 1224 Xintian, X.I.A., Minyong, W.E.N., Shaofeng, Z., Jing, H.E., Weitao, C., Affiliated, F., and Medicine,
1225 C. (2020). [An Increased Neutrophil/Lymphocyte Ratio Is an Early Warning Signal of Severe
1226 COVID-19]. *J South Med Univ* 40, 333–336.
- 1227 Xu, Z., Shi, L., Wang, Y., Zhang, J., Huang, L., Zhang, C., Liu, S., Zhao, P., Liu, H., Zhu, L., et al.
1228 (2020). Pathological findings of COVID-19 associated with acute respiratory distress syndrome.
1229 *Lancet Respir. Med.* 8, 420–422.
- 1230 You, Q., He, D.M., Shu, G.F., Cao, B., Xia, Y.Q., Xing, Y., Ni, M., Chen, J.F., Shi, S.L., Gu, H.F.,
1231 et al. (2019). Increased formation of neutrophil extracellular traps is associated with gut leakage
1232 in patients with type 1 but not type 2 diabetes. *J. Diabetes* 11, 665–673.
- 1233 Younos, I.H., Abe, F., and Talmadge, J.E. (2015). Myeloid-derived suppressor cells: Their role in
1234 the pathophysiology of hematologic malignancies and potential as therapeutic targets. *Leuk.*
1235 *Lymphoma*.
- 1236 Yu, G., Wang, L.G., Han, Y., and He, Q.Y. (2012). ClusterProfiler: An R package for comparing
1237 biological themes among gene clusters. *Omi. A J. Integr. Biol.* 16, 284–287.

- 1238 Zhang, N., Zhao, H., and Zhang, L. (2018). Fatty Acid Synthase Promotes the Palmitoylation of
1239 Chikungunya Virus nsP1. *J. Virol.* 93.
- 1240 Zhou, F., Yu, T., Du, R., Fan, G., Liu, Y., Liu, Z., Xiang, J., Wang, Y., Song, B., Gu, X., et al.
1241 (2020a). Clinical course and risk factors for mortality of adult inpatients with COVID-19 in
1242 Wuhan, China: a retrospective cohort study. *Lancet* 395, 1054–1062.
- 1243 Zhou, P., Yang, X. Lou, Wang, X.G., Hu, B., Zhang, L., Zhang, W., Si, H.R., Zhu, Y., Li, B., Huang,
1244 C.L., et al. (2020b). A pneumonia outbreak associated with a new coronavirus of probable bat
1245 origin. *Nature* 579, 270–273.
- 1246 Zhou, Z., Ren, L., Zhang, L., Zhong, J., Xiao, Y., Jia, Z., Guo, L., Yang, J., Wang, C., Jiang, S.,
1247 et al. (2020c). Overly Exuberant Innate Immune Response to SARS-CoV-2 Infection. *SSRN*
1248 *Electron. J.*
- 1249 Ziegler, C.G.K., Allon, S.J., Nyquist, S.K., Mbanjo, I.M., Miao, V.N., Tzouanas, C.N., Cao, Y.,
1250 Yousif, A.S., Bals, J., Hauser, B.M., et al. (2020). SARS-CoV-2 Receptor ACE2 Is an Interferon-
1251 Stimulated Gene in Human Airway Epithelial Cells and Is Detected in Specific Cell Subsets
1252 across Tissues. *Cell* 0.
- 1253 Ziying Ong, E., Fu Zi Chan, Y., Leong, W.Y., Mei Ying Lee, N., Kalimuddin, S., and Mohamed
1254 Haja Mohideen, S. (2020). A dynamic immune response shapes COVID-19 progression. *Cell* 0.
- 1255 Zuo, Y., Yalavarthi, S., Shi, H., Gockman, K., Zuo, M., Madison, J.A., Blair, C.N., Weber, A.,
1256 Barnes, B.J., Egeblad, M., et al. (2020). Neutrophil extracellular traps in COVID-19. *JCI Insight*.
1257

1258 **Acknowledgements**

1259 We thank Michael Kraut and Heidi Theis for technical assistance.

1260

1261

1262 **Deutsche COVID-19 Omics Initiative (DeCOI)**

1263 Robert Bals, Alexander Bartholomäus, Anke Becker, Ezio Bonifacio, Peer Bork, Thomas Clavel,
1264 Maria Colome-Tatche, Andreas Diefenbach, Alexander Dilthey, Nicole Fischer, Konrad Förstner,
1265 Julien Gagneur, Alexander Goesmann, Torsten Hain, Michael Hummel, Stefan Janssen, René
1266 Kallies, Birte Kehr, Andreas Keller, Sarah Kim-Hellmuth, Christoph Klein, Oliver Kohlbacher, Jan
1267 Korbel, Ingo Kurth, Markus Landthaler, Yang Li, Kerstin Ludwig, Oliwia Makarewicz, Manja Marz,
1268 Alice McHardy, Christian Mertes, Markus Nöthen, Peter Nürnberg, Uwe Ohler, Stephan
1269 Ossowski, Jörg Overmann, Klaus Pfeffer, Alfred Pühler, Nikolaus Rajewsky, Markus Ralser, Olaf
1270 Rieß, Stephan Ripke, Ulisses Nunes da Rocha, Philip Rosenstiel, Antoine-Emmanuel Saliba, Leif
1271 Erik Sander, Birgit Sawitzki, Philipp Schiffer, Joachim L. Schultze, Alexander Sczyrba, Oliver
1272 Stegle, Jens Stoye, Fabian Theis, Janne Vehreschild, Jörg Vogel, Max von Kleist, Andreas
1273 Walker, Jörn Walter, Dagmar Wieczorek, John Ziebuhr

1274

1275

1276 **Funding**

1277 This work was supported by the German Research Foundation (DFG, SFB-TR84 #114933180 to
1278 L.E.S., S.H., A.H., N.S., C.D.; INST 37/1049-1, INST 216/981-1, INST 257/605-1, INST 269/768-
1279 1 and INST 217/988-1, INST 217/577-1 to J.L.S.; SFB TR57, SPP1937 to J.N.; GRK2157 to A.-
1280 E.S., ME 3644/5-1 to H.E.M.); the Berlin University Alliance (BUA, PreEP-Corona grant to L.E.S.
1281 , V.C. and C.D.), the Berlin Institute of Health (BIH, grant to L.E.S., A.H., C.D.); the HGF grant
1282 sparse2big, the EU projects SYSCID (grant number 733100), and ERA CVD (grant number
1283 00160389) to J.L.S.; the DZIF (TTU 04.816, 04.817 to J.N.); the Hector-Foundation (M89 to J.N.);
1284 the EU projects ONE STUDY (grant number 260687 to B.S.), BIO-DrIM (305147 to B.S.) and
1285 INsTRuCT (grant number 860003 to B.S.), the German Federal Ministry of Education and
1286 Research (BMBF, project RAPID to C.D., S.H., A.H.), and a Charité ³R project to B.S. and S.H.;
1287 Radboud University Medical Centre Hypatia Grant (2018 to Y.L.).

1288

1289 **Declaration of interests**

1290 The authors do not declare any conflict of interest

1291

1292 **Author contributions**

1293 Conceptualization: J. S-S., N.R., K.B., B.K., L.B., F.K., J.L.S, A.C.A., Y.L., J.N., B.S., A.-E.S., L.E.S.

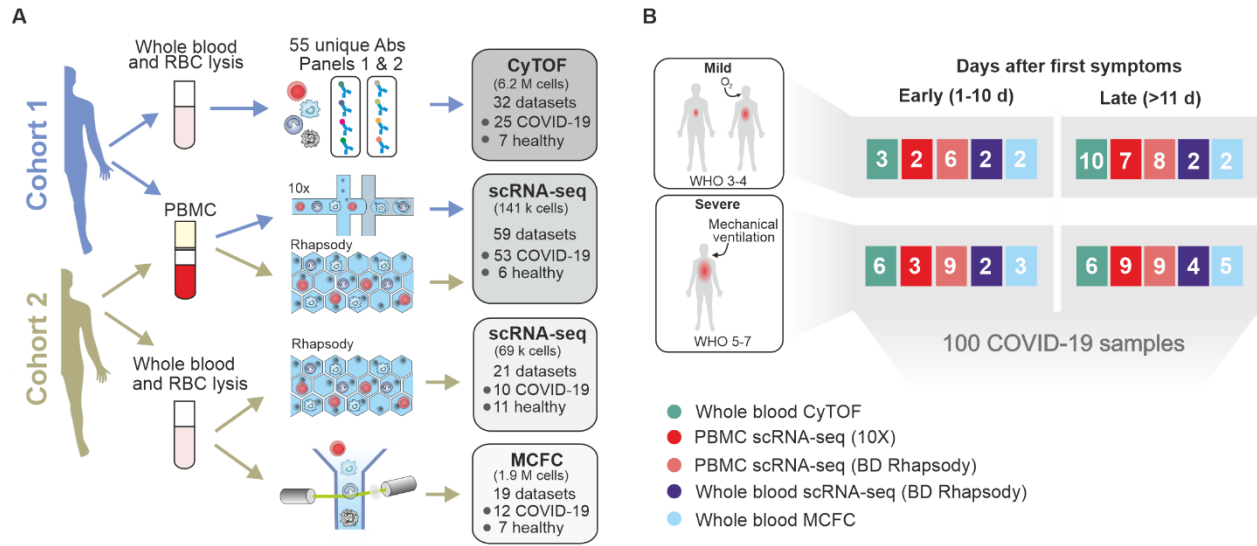
1294 Methodology: J. S-S., D.P., T.K., S.B., L.B., E.D.D., M.G., D.W., M.B., T.S.K., A.S., O.D., H.M., A.R.S,

1295 C.C., D.K., E.V., C.J.X., A.D., C.T., S.H., C.L.G., T.U., M.B., R.G., C.D., C.V.K., K.H. Software/data
1296 analysis: J. S-S., N.R., K.B., S.S., B.Z., T.K., L.B., A.S., T.U., M.B. Investigation: J. S-S., K.B., T.P., A.H.,
1297 M.H., J.L.S, A.C.A., M.W., Y.L., J.N., B.S., A.-E.S., L.E.S. Biospecimen/ enzyme resources: B.K., S.B.,
1298 M.P., S.H., H.M.R., F.M., A.U., L.B.J., L.J., C.R.G., J.R., K.M.K, M.T., G.R., F.K., J.N., M.W. Writing –
1299 Original Draft: J. S-S., N.R., K.B., L.B., E.D.D., C.M., J.L.S, A.C.A., Y.L., J.N., B.S., A.-E.S., L.E.S. Writing
1300 – Review & Editing: J. S-S., N.R., M.W., K.B., L.B., E.D.D., T.P., M.B., T.S.K., S.H., A.H., M.S., H.D.V.,
1301 C.D., N.S., C.V.K., F.K., J.L.S, A.C.A., Y.L., J.N., B.S., A.-E.S., L.E.S.

1302

1303 **Figures, figure titles and legends**

Figure 1



1304

1305

1306 **Figure 1. Cohort definition and single-cell multi-omics analysis strategy.**

1307 **A**, Processing pipeline for healthy and COVID-19 blood samples strategies used in this study.
1308 PBMC are isolated after Ficoll, labeled with cell hashing antibodies and loaded on a droplet-based
1309 single-cell RNA-seq (scRNA-seq) platform. Red blood cells (RBC) are lysed and immune cells
1310 are labeled with two panels of metal-labeled antibodies and processed with CyTOF platform.
1311 Number of subjects analyzed for each cohort included in this study is summarized on the right
1312 boxes.

1313 **B**, Features of the cohort classified according to WHO-defined clinical grades (3 to 8) and the
1314 time after first symptoms.

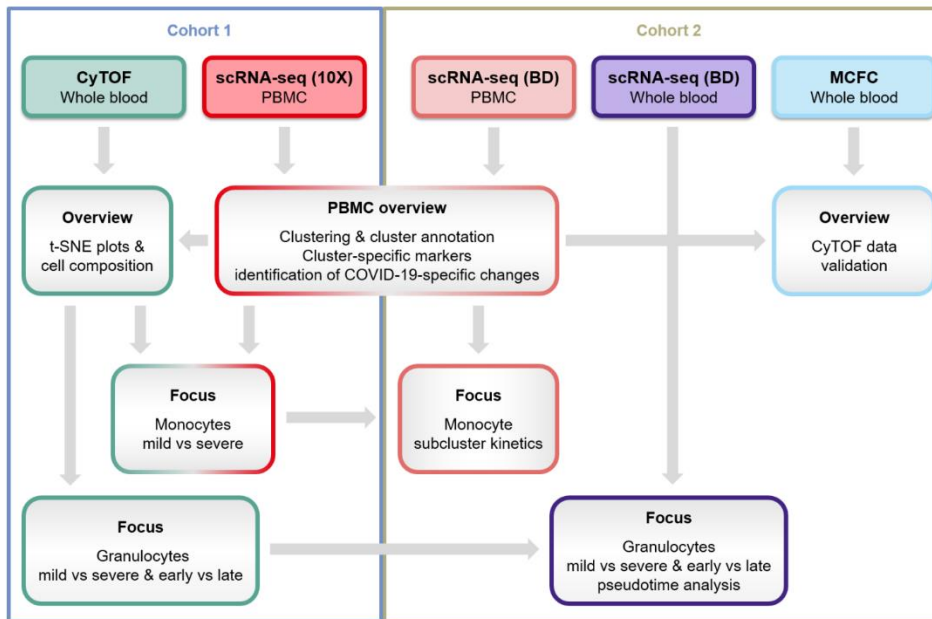
1315 **C**, Visualization of t-distributed stochastic neighbor embedding (tSNE)-automated analysis of
1316 CD45+ leukocytes, down-sampled to 70,000 cells, from our mass cytometry analyses using
1317 antibody panel 2 based on similarities in expression of 29 markers as defined in supplementary
1318 table 2. Cells are colored according to donor origin (blue = healthy controls, yellow = mild COVID-
1319 19, red = severe COVID-19) and major lineage subtypes.

1320 **D**, Box plots summarising differences in major immune cell lineage subtype composition of whole
1321 blood samples from COVID-19 patients with mild (n=5) or severe disease (n=6) course, age-
1322 matched healthy controls utilized in mass cytometry (HC CyTOF, n=7) or measured by
1323 conventional or multi-colour flow cytometry (HC flow, n=18) as previously reported (Kverneland
1324 et al., 2016). * $p < 0.05$, ** $p < 0.01$, *** $p < 0.001$

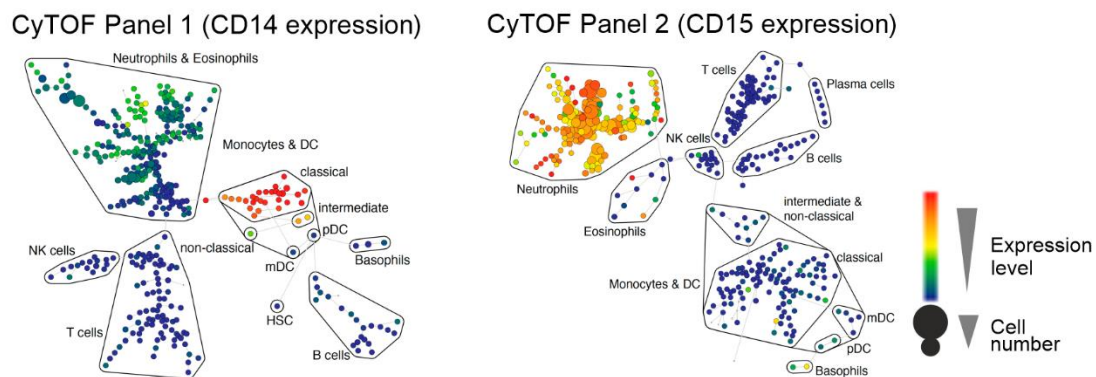
1325

Supplemental Figure 1

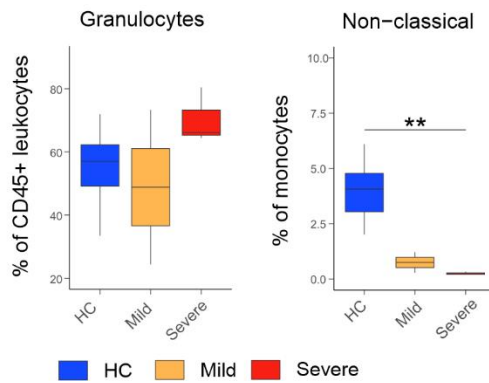
A



B



C



1326

1327 **Supplemental Figure 1. Overview of sample analysis pipeline, major leukocyte lineages**
1328 **definition and quantification by CyTOF and MCFC.**

1329 **A**, Overview summarising sample analysis pipeline for single cell transcriptomics and proteomics
1330 of COVID-19 samples.

1331 **B**, High resolution SPADE analysis with 400 target nodes and individual nodes aggregated to the
1332 indicated major immune cell lineages according to the expression of lineage specific cell marker
1333 such as CD14 for monocytes and CD15 for neutrophils of whole blood samples collected from
1334 COVID-19 patients and healthy controls and stained with CyTOF panel 1 and 2, respectively.

1335 **C**, Box plots summarising differences in major immune cell lineage subtype composition of whole
1336 blood samples from the second cohort of COVID-19 patients showing either mild (n=2) or
1337 severe/critical disease (n=3) course, age-matched healthy controls (n=7) measured by
1338 conventional fluorochrome-based cytometry. **p<0.01.

1339

1341 **Figure 2. scRNA-seq of PBMC from patients of two independent cohorts reveals dynamic**
1342 **changes in the composition and the transcriptional states of myeloid cells in the**
1343 **peripheral blood in COVID-19**

1344 Abbreviations: HC: Healthy control.

1345 **A**, UMAP visualization of 10x chromium scRNA-seq profiles of 48,085 PBMC purified by density
1346 gradient centrifugation of peripheral blood from 21 samples of different time points of 4 mild
1347 and 8 severe patients in cohort 1 colored according to the indicated cell type classification based
1348 on Louvain clustering, reference-based cell-type annotation and marker gene expression
1349 patterns.

1350 **B**, UMAP shown in (a) colored according to disease severity (yellow = mild COVID-19, red =
1351 severe COVID-19).

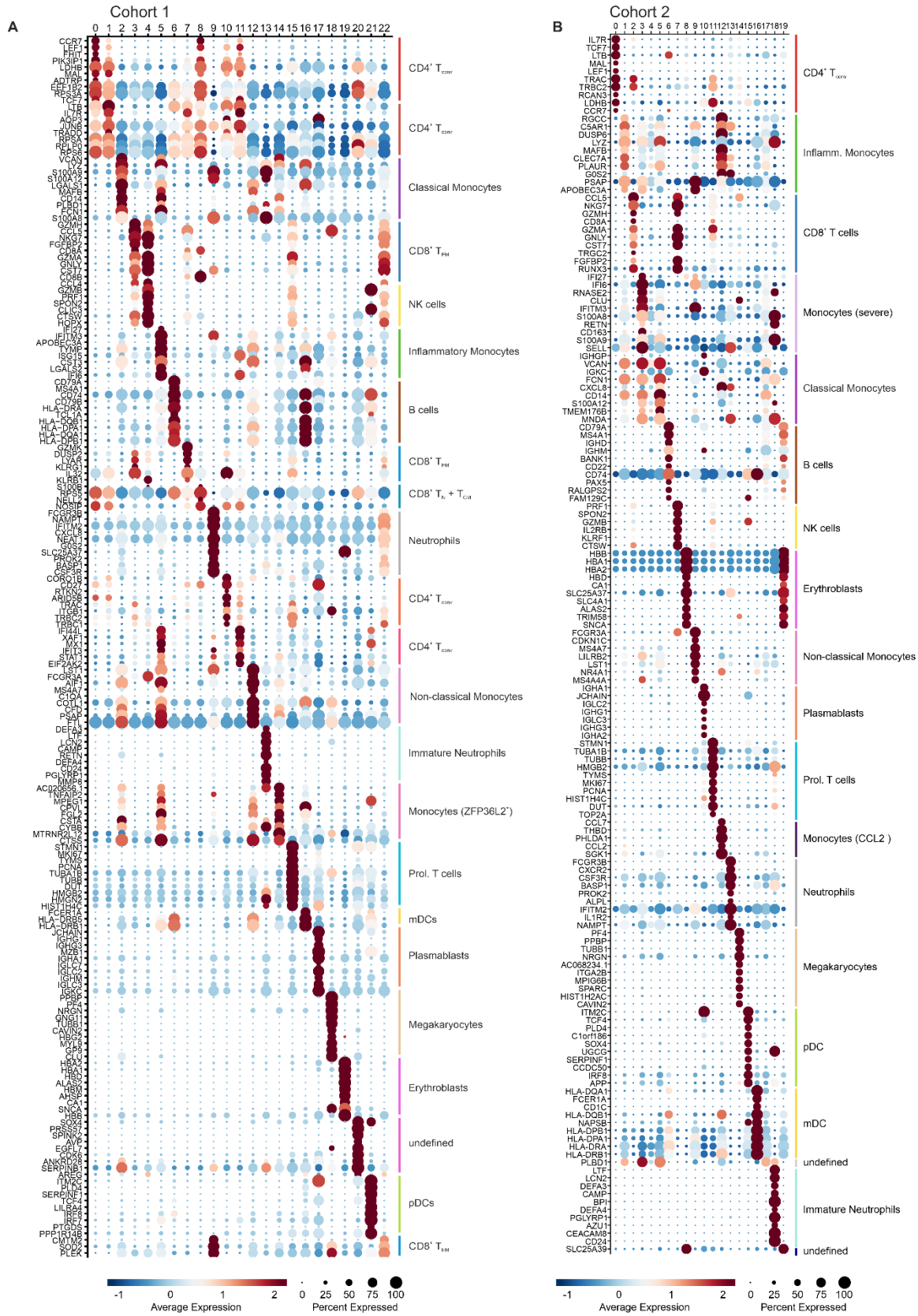
1352 **C**, Dot plot representation of the top 10 marker genes sorted by average log fold change
1353 determined for the indicated myeloid cell subsets in the PBMC data set of cohort 1 plotted across
1354 the subsets of both cohorts.

1355 **D**, UMAP visualization of BD rhapsody scRNA-seq profiles of 93,297 PBMC purified by density
1356 gradient centrifugation from peripheral blood from 35 samples of 6 mild and 5 severe and 2 control
1357 patients of different time points in cohort 2 colored according to the indicated cell type
1358 classification based on Louvain clustering, reference-based cell-type annotation and marker gene
1359 expression patterns (Suppl. Fig. 2A).

1360 **E**, Box plots visualizing the percentages of the indicated cell subsets of the total number of PBMCs
1361 assessed per patient in the respective data set. Boxes are colored according to disease group
1362 and dots according to the respective cohort of the sample. For neutrophils and immature
1363 neutrophils only fresh PBMC samples were included.

1364

Supplemental Figure 2



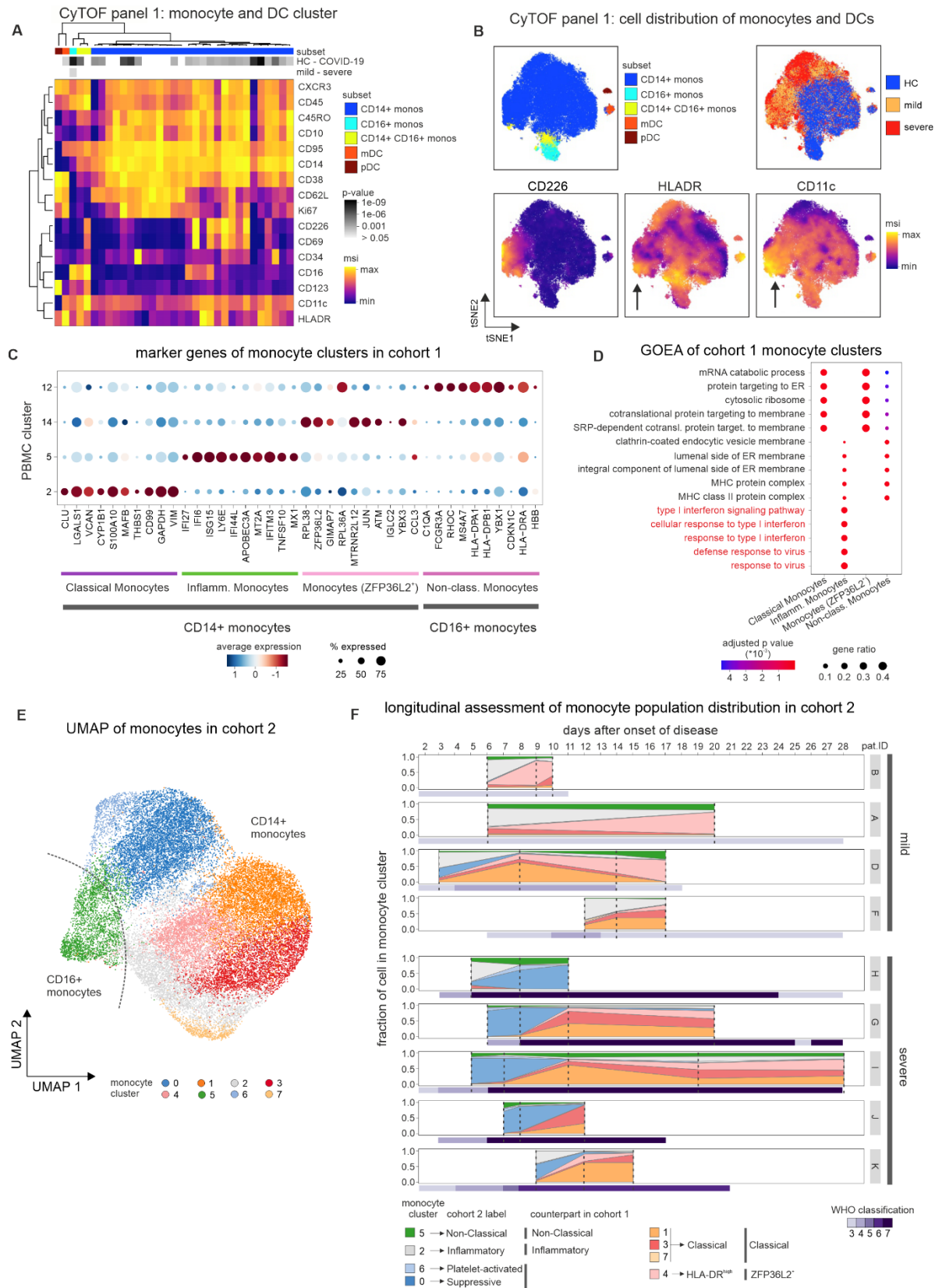
1366 **Supplemental Figure 2. Cluster-specific marker gene expression shows inflammatory**
1367 **activation signatures of monocyte subsets and the appearance of neutrophil subsets in**
1368 **the PBMC fraction**

1369 **A**, Dot plot representation of the top 10 marker genes sorted by average log fold change
1370 determined for the clusters depicted in the UMAP in Figure 2A.

1371
1372 **B**, Dot plot representation of the top 10 marker genes sorted by average log fold change
1373 determined for the clusters depicted in the UMAP in Figure 2C.

1374

Figure 3



1376 **Figure 3. Subjects with different COVID-19 stages display unique phenotypical and**
1377 **transcriptional monocyte signatures.**

1378 **A**, Heatmap revealing differences in marker expression determined by mass cytometry (CyTOF)
1379 using antibody panel 1 of monocyte and dendritic cell cluster. Cell clusters are displayed in
1380 columns and marker identity is indicated in rows. MSI = marker staining intensity respective
1381 expression level, significance level for the comparisons i) healthy controls (HC, n=7) versus
1382 COVID-19 (upper row) as well as ii) mild (n=5) versus severe (n=6, lower row) are indicated using
1383 a grey scale on top of the heatmap.

1384 **B**, t-SNE plots of monocytes and dendritic cells, down-sampled to 70,000 cells, based on their
1385 similarities in expression of 35 markers as defined in supplementary table 2. Cells are colored
1386 according to parental subclusters (classical monocytes, non-classical monocytes, intermediate
1387 monocytes, myeloid dendritic cells, plasmacytoid dendritic cells), donor origin (blue = healthy
1388 controls, yellow = mild COVID-19, red = severe COVID-19) and expression intensity of CD226,
1389 HLA-DR and CD11c.

1390 **C**, Dot plot representation of marker genes calculated for the clusters within the monocyte
1391 space of cohort 1.

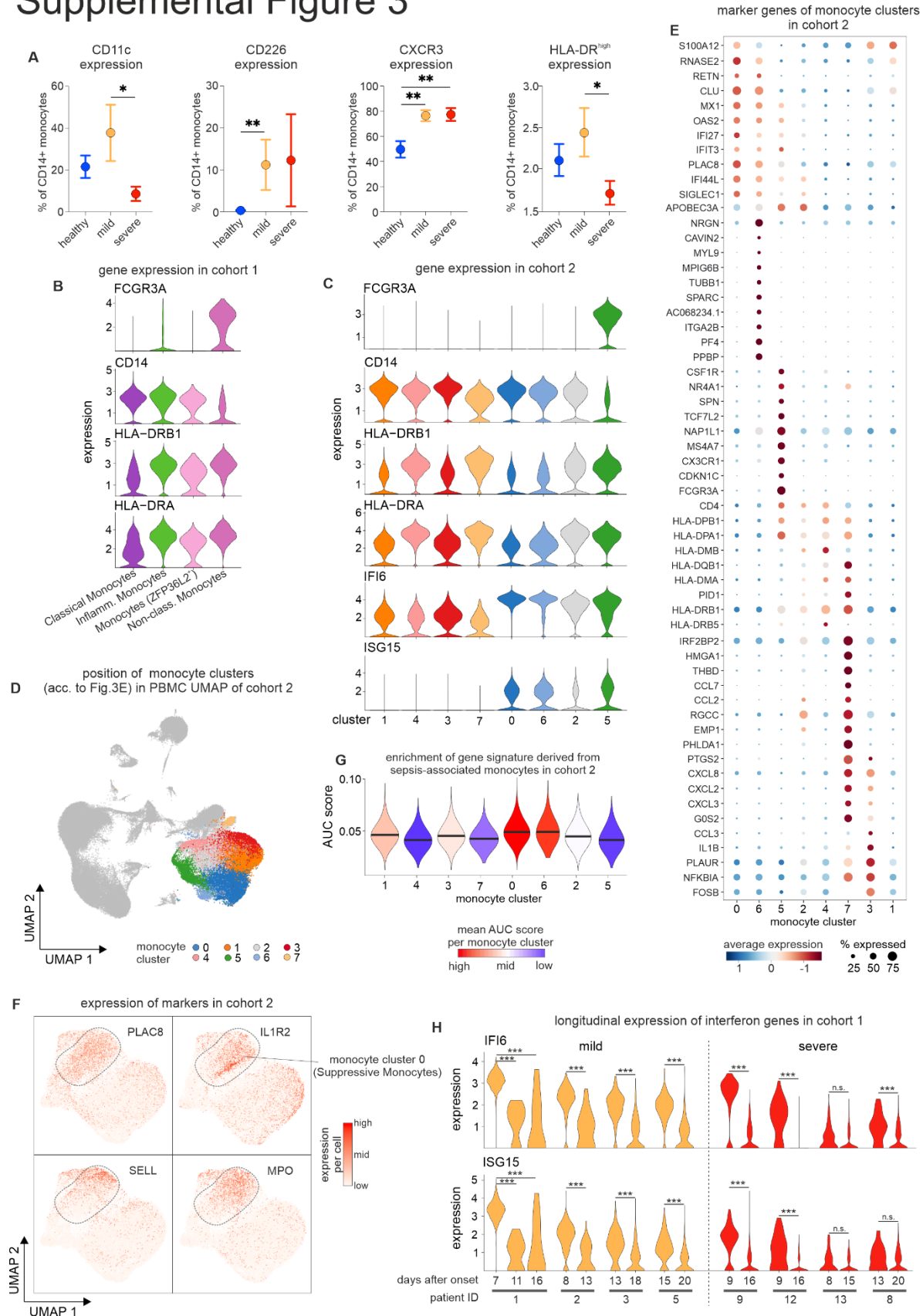
1392 **D**, Gene ontology enrichment analysis of complete marker genes obtained for each identified
1393 monocyte population of cohort 1.

1394 **E**, UMAP visualization of 29,334 cells within the monocyte space of cohort 2. Cells are colored
1395 according to the identified clusters.

1396 **F**, Cluster occupancy per patient over time. Coloring according to the clusters identified in
1397 Figure 3E. Vertical dashed lines indicate the time points at which the samples were taken. The
1398 violet bar below the individual patient data indicates the respective WHO classification. Patient
1399 IDs are shown on the right.

1400

Supplemental Figure 3



1402 **Supplemental Figure 3. Phenotypical and transcriptional differences of monocytes from**
1403 **mild and severe COVID-19**

1404 **A**, Box plots summarizing differences in CD226, HLA-DR^{high}, CD11c and CXCR3 expression
1405 within classical monocytes measured by mass cytometry in whole blood samples from cohort 1
1406 distinguishing between healthy controls (n=7), COVID-19 patients with mild (n=5) or
1407 severe/critical disease (n=6) course. *p<0.05, **p>0.01

1408 **B**, Violin plots representing expression of selected genes in monocyte clusters of cohort 1.
1409 Coloring according to cluster color in Figure 2

1410 **C**, Violin plots representing expression of selected genes in monocyte clusters of cohort 2.

1411 **D**, Back mapping of identified monocyte clusters of cohort 2 onto the PBMC UMAP in Figure 2.

1412 **E**, Dot plot representation of marker genes found in monocyte clusters of cohort 2.

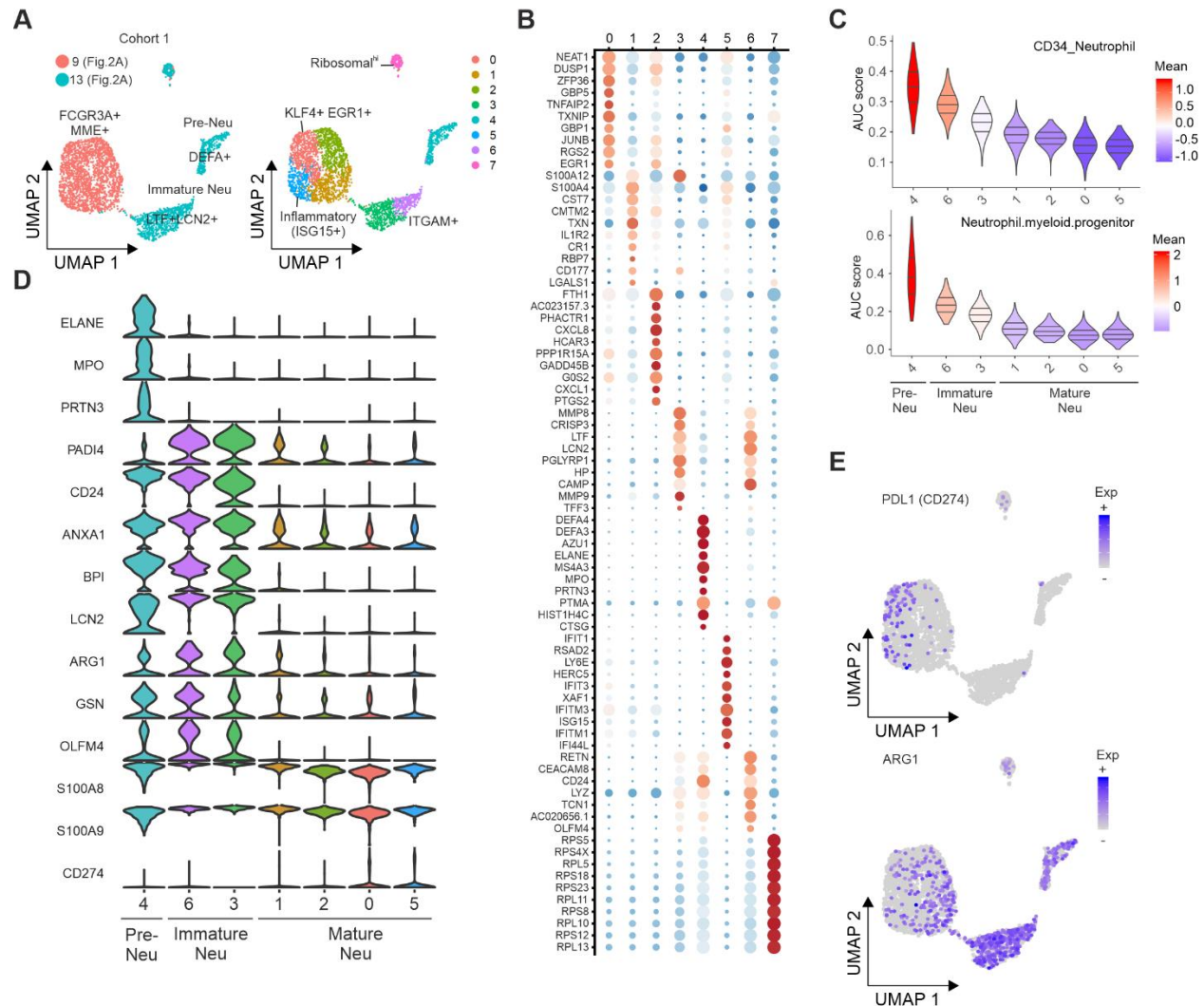
1413 **F**, Visualization of the expression of selected genes in the UMAP of the monocyte space in cohort
1414 2.

1415 **G**, AUC_{Cell}-based enrichment of gene signature derived from sepsis-associated monocytes
1416 (Reyes et al., 2020) in monocytes of cohort 2 and plotting of the 'Area Under the Curve' (AUC)
1417 scores as violin plots. The horizontal lines in the violin plots represent the median of the respective
1418 AUC scores per cluster.

1419 **H**, Time-dependent change of IFI6 and ISG15 expression in monocytes of cohort 1. Significant
1420 changes determined by the Wilcoxon rank sum test are indicated (***) = pvalue < 0.001; n.s. = not
1421 significant).

1422

Figure 4



1423

1424 **Figure 4. Immature and dysfunctional low-density neutrophils emerge in PBMC fractions.**

1425 **A**, UMAP representation and clustering of the neutrophils identified in PBMC from cohort 1
 1426 (clusters 9 and 13 in Figure 2A).

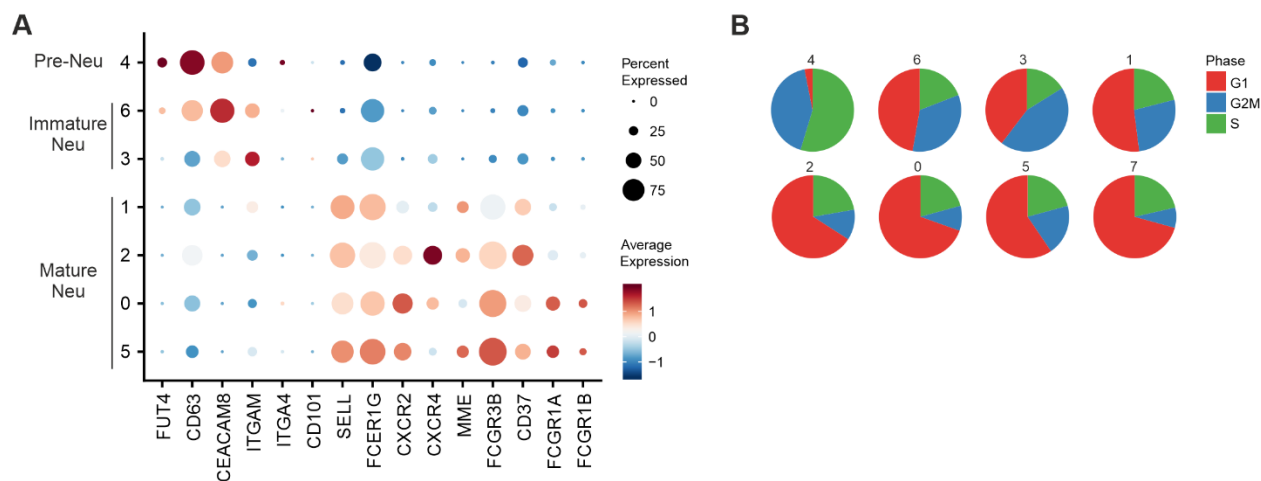
1427 **B**, Dot plot visualization of the expression of the cluster-specific marker genes associated to
 1428 each of clusters identified in panel A.

1429 **C**, Signature enrichment score of neutrophil progenitors derived from previous single-cell data.
 1430 AUC: Area under the curve.

1431 **D**, Violin plots giving the expression of selected activation genes across the neutrophil clusters
 1432 identified in panel A.

1433 **E**, Expression of ARG1 and PD-L1 projected on the UMAP from panel A.

Supplemental Figure 4



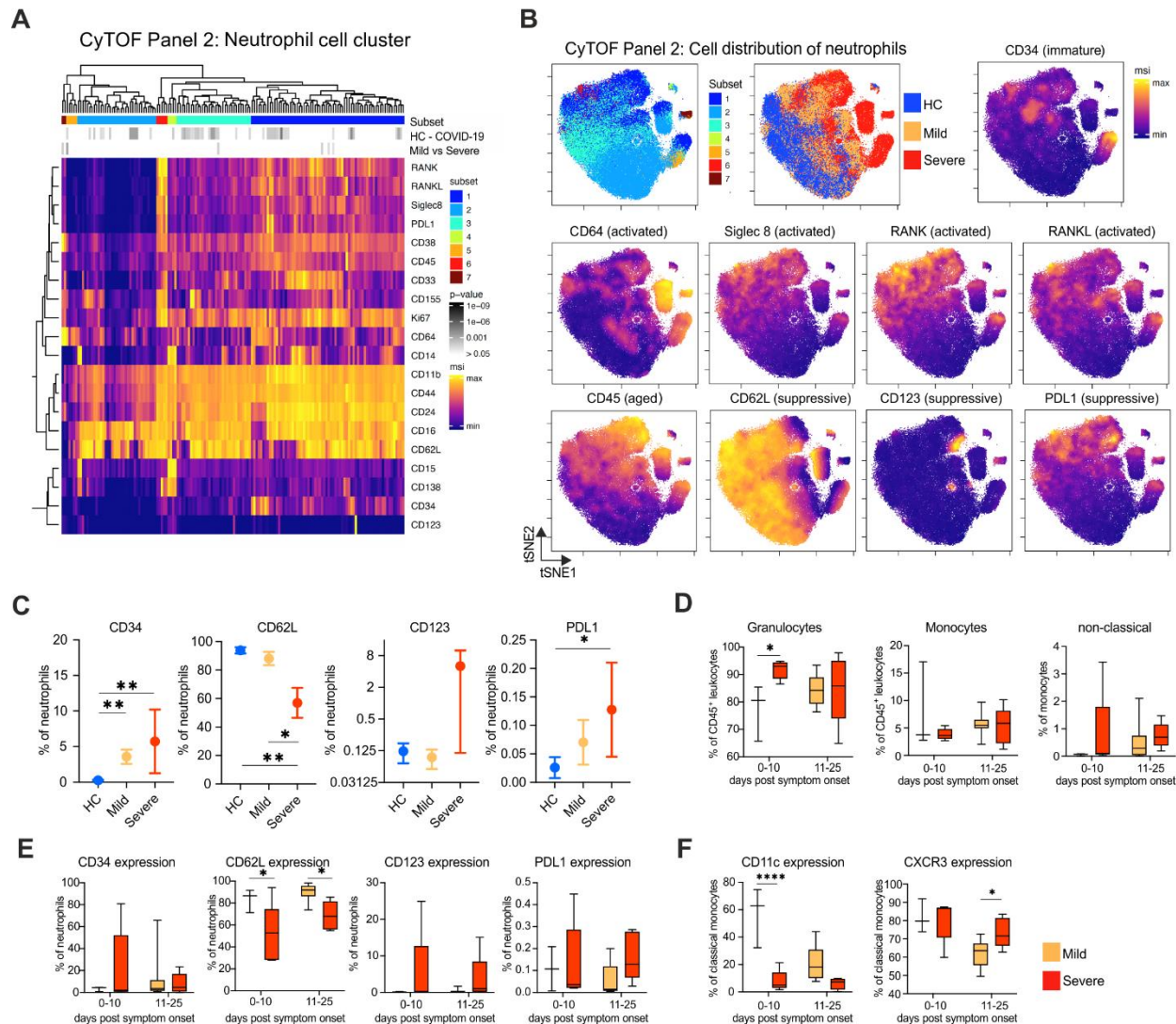
1434
1435
1436
1437
1438

Supplemental Figure 4. Additional analysis of dysfunctional neutrophils in PBMC fraction.

1439 **A**, Dot plot representation of marker genes associated to pre-neutrophils (pre-neutr), immature
1440 and mature neutrophils.

1441 **B**, Pie charts giving the proportion of cells in each cell cycle stage. The numbers refer to
1442 clusters as identified in the UMAP in Figure 4A.

Figure 5



1443

1444

1445 **Figure 5. Disbalance between increase in activated and potentially immunosuppressive**
 1446 **neutrophils discriminates between mild and severe COVID-19 patients.**

1447 **A**, Heatmap revealing differences in marker expression determined by mass cytometry (CyTOF)
 1448 using antibody panel 2 of identified neutrophil cell subcluster (1 to 7). Neutrophil cell clusters
 1449 belonging to the identified subcluster are displayed in columns and marker identity is indicated in
 1450 rows. MSI = marker staining intensity respective expression level, significance level for the
 1451 comparisons i) healthy controls (HC) versus COVID-19 (upper row) as well as ii) mild versus
 1452 severe (lower row) are indicated using a grey scale on top of the heatmap.

1453 **B**, t-SNE plots of neutrophils, down-sampled to 70.000 cells, based on their similarities in
 1454 expression of 29 markers as defined in supplementary table 2. Cells are colored according to

1455 neutrophil subcluster, donor origin (blue = healthy controls, yellow = mild COVID-19, red = severe
1456 COVID-19) and expression intensity of CD34, CD64, Siglec 8, RANK, RANKL, CD45, CD62L,
1457 CD123 and PD-L1.

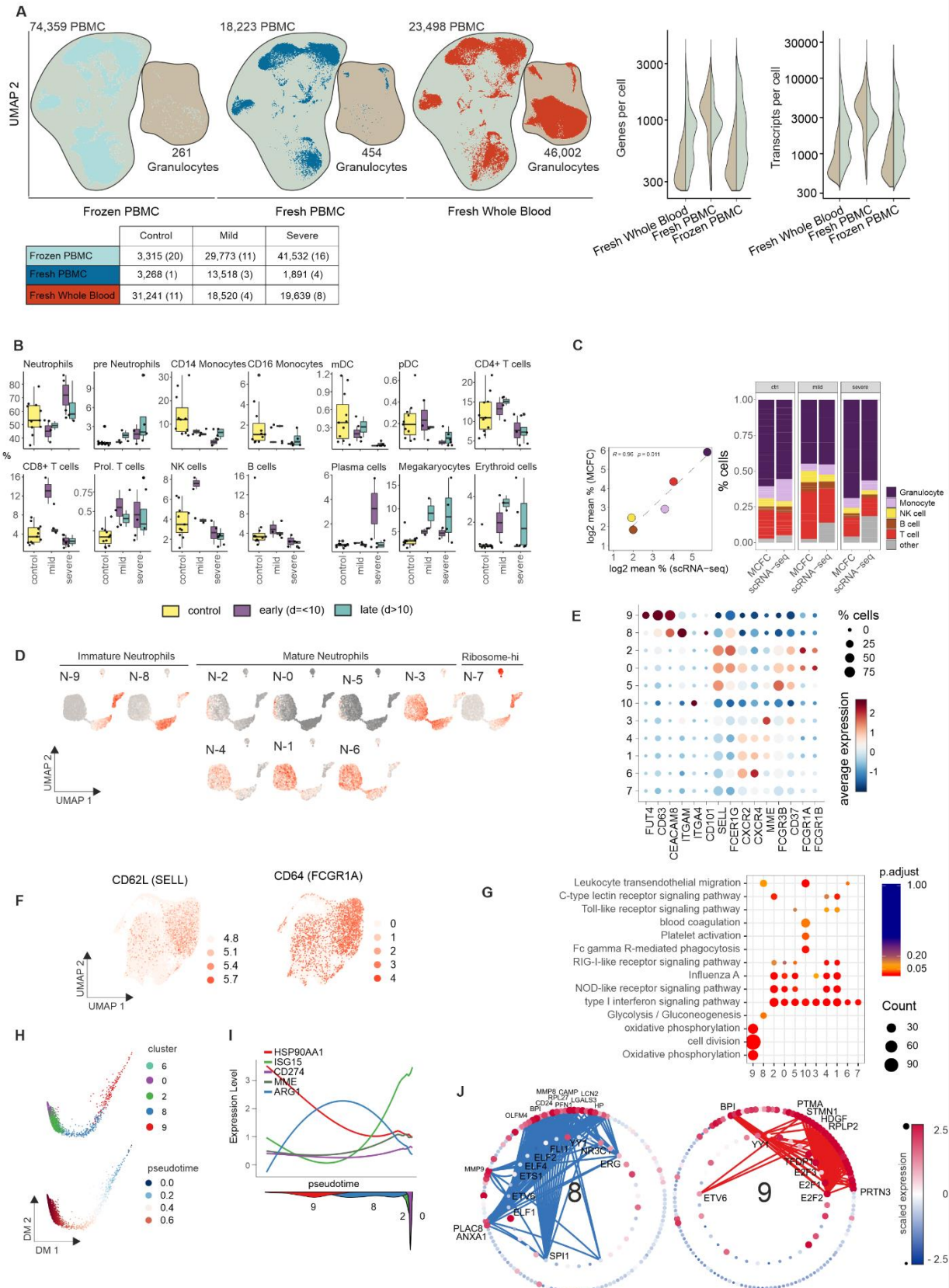
1458 **C**, Bar graphs summarizing CD34, CD62L, CD123 and PD-L1 expression as % positive cells
1459 within neutrophils of whole blood samples from COVID-19 patients with mild (n=5) or severe
1460 disease (n=5) course and age-matched healthy controls (n=7). *p<0.05, **p<0.01

1461 **D-F**, Box plots summarizing time-dependent differences in total granulocytes and monocytes,
1462 non-classical monocytes (**D**) CD34, CD62L, CD123 and PD-L1 expressing neutrophils (**E**) as well
1463 as CD11c and CXCR3 expressing classical monocytes (**F**) measured by mass cytometry in whole
1464 blood samples from cohort 1 distinguishing between COVID-19 patients with mild (days 0-10:
1465 n=3, days 11-25: n=10) or severe/critical disease (days 0-10: n=5, days 11-25: n=5) course.
1466 *p<0.05, ****p<0.0001

1467

- 1469 **Figure 6. Delineation of suppressive mature neutrophils in late stage severe COVID-19.**
- 1470 **A**, UMAP visualization of fresh blood samples from cohort 2 (PBMC and whole blood combined,
1471 88,177 cells, controls (ctrl = 12), COVID-19 mild (mild = 6), COVID-19 severe (severe = 8).
- 1472 **B**, UMAP visualization of the immature and mature neutrophils (30,019 cells) from Figure 6A after
1473 exclusion of one experimental batch (see Methods, controls (ctrl = 10), COVID-19 early mild = 1,
1474 COVID-19 severe (early = 2, late = 2)).
- 1475 **C**, Dot plot of selected top 6 marker genes ordered by average log fold-change highlighting the
1476 heterogeneity of the neutrophil space in b.
- 1477 **D**, Overview of functional nomenclature and marker genes for each cluster in the neutrophil space
1478 in COVID-19 and control patients.
- 1479 **E**, UMAP visualization of neutrophils showing the scaled expression of PD-L1 (*CD274*) with a
1480 clear enrichment in the Covid-19 specific clusters 2 and 0.
- 1481 **F**, Confusion matrix for each cluster in Figure 6B divided by disease severity and time point
1482 showing the enrichment of each patient group for each cluster; the scale is normalized for each
1483 cluster.
- 1484 **G**, Density plot of cell frequency by disease severity and time point overlaid on UMAP visualization
1485 of the neutrophil space.
- 1486 **H**, Dot plot of genes from different functional classes showing the differences of the neutrophil
1487 states (based on literature research).
- 1488 **I**, Transcription factor binding prediction results for clusters 0, 2 and 5 shown as networks of
1489 transcription factors and their targets among the specifically expressed genes for the given
1490 cluster. Edges represent predicted transcriptional regulation. Transcription factors in the inner
1491 circle and their predicted target genes in the outer circle are represented as nodes sized and
1492 colored according to the scaled expression level across all clusters. Top 10 highest connected
1493 transcription factors and those exclusively predicted for the cluster as well as the top 5 highest
1494 connected target genes together with a literature-based selection of targets are labeled.
- 1495

Supplemental Figure 6



1497 **Supplemental Figure 6. Overview of scRNA-seq dataset from cohort 2 and additional**
1498 **characterization of suppressive neutrophils.**

1499 **A**, UMAP (right) of the complete scRNA-seq dataset from cohort 2 (frozen PBMC, fresh PBMC,
1500 fresh whole blood) and violin plot of number of genes and transcripts expressed in the PBMC VS.
1501 granulocyte fraction across the different data sets of cohort 2 (right). Violin plots are split into
1502 granulocytes (left) and PBMC (right). The table below indicates the number of cells per
1503 experimental condition with the number of samples in brackets.

1504 **B**, Box plot of cell type frequencies identified by scRNA-seq in fresh whole blood samples after
1505 erythrocyte lysis comparing 23 samples from 11 control individuals, 4 samples from mild and 8
1506 samples from severe COVID-19 patients at early and late timepoints.

1507 **C**, Comparison between cell frequencies identified by scRNA-seq and MCFC, pearson's
1508 correlation between the mean of each cell population (left) and stacked bar chart sorted by
1509 disease severity.

1510 **D**, Enrichment of signature genes from the neutrophil clusters from cohort 2 on the UMAP
1511 visualization of cohort 1.

1512 **E**, Dot plot representation of marker genes taken from literature classifying different neutrophil
1513 subsets.

1514 **F**, UMAP representation of neutrophils showing the scaled expression of CD62L (*SELL*) and
1515 CD64 (*FCGR1A*) with a clear enrichment in the COVID-19 specific clusters 2 and 0.

1516 **G**, Dot plot visualization of selected significantly enriched Gene Ontology terms and KEGG
1517 pathways for each cluster from the neutrophil space.

1518 **H**, Diffusion map dimensionality reduction of the main neutrophil clusters 9, 8, 2, 0 and 6 from the
1519 severe COVID-19 patients (top) and diffusion pseudotime visualized on the diffusion map
1520 indicating the transition probability of the different clusters in the following order: 9 - 8 - 2 - 0 - 6
1521 (bottom).

1522 **I**, Genes specific for each cluster visualized along the diffusion pseudotime (top) with the density
1523 of each cluster along the pseudotime (bottom) highlighting the proposed order of differentiation of
1524 the different neutrophil subsets.

1525 **H**, Transcription factor binding prediction results for clusters 8 and 9 shown as networks of
1526 transcription factors and their targets among the specifically expressed genes for the given
1527 cluster. Edges represent predicted transcriptional regulation. Transcription factors in the inner
1528 circle and their predicted target genes in the outer circle are represented as nodes sized and
1529 colored according to the scaled expression level across all clusters. Top 10 highest connected
1530 transcription factors and those exclusively predicted for the cluster as well as the top 5 highest
1531 connected target genes together with a literature-based selection of targets are labeled.

1532 **Supplemental Tables**

1533

1534 **Supplemental Table 1. Cohort outline used to perform scRNA-seq, mass cytometry and**
1535 **MCFC (multi-colour flow cytometry).**

1536

1537 **Supplemental Table 2. Detailed information on antibody panels used for mass cytometry**
1538 **analysis.**

1539

1540 **Supplemental Table 3. List of antibodies used for MCFC.**